# FOURTH SEMI-ANNUAL PROGRESS REPORT

NASA GRANT NAG8-950

# CONVECTIVE FLOW EFFECTS ON PROTEIN CRYSTAL GROWTH

Period of Performance
8/1/94 through 1/31/95



Principal Investigator
FRANZ ROSENBERGER

Co-Investigator
LISA A. MONACO

Center for Microgravity and Materials Research
University of Alabama in Huntsville
Huntsville, Alabama 35899

## *1. Introduction*

During the fourth semi-annual period under this grant we have pursued the following activities:

- Crystal growth morphology and kinetics studies with tetragonal lysozyme. These clearly revealed the influence of higher molecular weight protein impurities on interface shape; see the attached preprint.
- Characterization of the purity and further purification of lysozyme solutions. These efforts have, for the first time, resulted in lysozyme free of higher molecular weight components; see Section 2.
- Continuation of the salt repartitioning studies with Seikagaku lysozyme, which is has a lower protein impurity content than Sigma stock. These efforts confirmed our earlier findings of higher salt contents in smaller crystals. However, less salt is in corporated into the crystals grown from Seikagaku stock. This strongly suggests a dependence of salt repartitioning on the concentration of protein impurities in lysozyme. To test this hypothesis, repartitioning studies with the high purity lysozyme prepared in-house will be begun shortly.
- Numerical modelling of the interaction between bulk transport and interface kinetics. These simulations have produced interface shapes which are in good agreement with our experimental observations; see Section 3.
- Light scattering studies on under- and supersaturated lysozyme solutions. A consistent interpretation of the static and dynamic data leaves little doubt that pre-nucleation clusters, claimed to exist even in undersaturated solutions, are not present; see Section 4.

## *2. Protein characterization and purification*

*Electrophoretic Analysis*

Both of the commercial available hen-egg white lysozyme stocks studied thus far, Sigma and Seikagaku, contain a 30 kD molecular weight impurity and to a lesser extent, higher molecular weight impurities ranging from 50 to 94 kD. Although a strict quantitative analysis of the impurities has yet to be done, it is apparent that Seikagaku is the purer stock. This statement is based on the appearance of a strong higher molecular weight banding pattern found in Sigma lysozyme solutions.

In order to maximize the analytical sensitivity, all gels were heavily over-loaded (above maximum amount of protein necessary for detection) and silver-stained.

*Chromatographic Analysis*

Lysozyme has a relatively unique isoelectric point (pI) of 10.8, therefore the obvious approach to purifying lysozyme would appear to be applying the protein to a cation exchange

column at a pH lower then its pI. At a pH below that of lysozyme's pI the protein should carry an overall positive charge and be attracted to the negatively charged resin of the cation exchange column. Since most proteins have a pI in the range of 4 to 7, by maintaining a pH of ~ 5 one would expect that the impurities would be weakly, if at all, attracted to the resin and elute in a buffer of low ionic strength. Lysozyme, on the other hand, should be strongly attracted to the resin and elute off the column at a high ionic strength. What was found was strikingly different to the this expectation.

The majority of lysozyme coeluted with the 30 kD molecular weight impurity off a cation exchange column with a salt gradient elution, independent of several pHs used ranging from 4.5 to 8.0. Only at pH 7.0 there appeared to be a slight improvement in the resolution of the shoulder and tail portion of the dominant peak.

Since this approach did not offer a productive means for lysozyme purification, alternative methods are now being employed. Two of the methods used in combination with ion exchange column chromatography include 1) dialyzing the lysozyme solution against urea which would result in protein unfolding and 2) incubating the lysozyme solution with trypsin, a known protease. Both methods, besides purifying lysozyme, are also expected to result in a subsequent loss of native lysozyme. The third alternative is co-crystallization of the lysozyme solution in the presence of hen egg white anti-lysozyme. The anti-lysozyme may be able to effectively compete and hinder the binding of the impurity with lysozyme.

The first method, dialyzing lysozyme against urea, was not successful in separating the 30 kD impurity from lysozyme. Following a 2.5 day dialysis against 5 M urea, the protein solution was applied to a cation exchange column and eluted with a 5 M urea/1 M NaCl buffer gradient. The experiment was to unfold the protein(s), separate the unfolded proteins using cation exchange chromatography and then pool the individual peaks and dialyze to induce refolding. Even under 5 M urea conditions, coelution still occurred when the peaks were analyzed electrophoretically.

All purification methods performed thus far, have involved the use of salt (e.g. 3-6x recrystallization, column chromatography using salt gradient elution, protein unfolding followed by chromatography using salt gradient elution). With the idea that salt may facilitate the affinity of the 30 kD molecular weight impurity for lysozyme, a purification method without the use of salt was employed.

This method involved again, cation exchange chromatography, but instead of a salt gradient elution a pH elution was utilized. The cation exchange column was equilibrated at a pH of 4.5 (0.1 M $NaH_2PO_4$). The lysozyme solution was prepared and applied on the column at pH 4.5 (0.1 M $NaH_2PO_4$). The column was eluted isocratically with a pH of 9.0 (0.1 M $Na_2HPO_4$). The chromatogram exhibited the previously seen major peak but the shoulder portion had several

defined small peaks not seen with the previous techniques. When examined electrophoretically, the isocratic pH elution was found to be successful in separating the 30 kD molecular weight impurity from lysozyme. The shoulder portion of the major peak contained the majority of the 30 kD molecular weight impurity complexed to lysozyme and the remaining portion of the peak consisted of pure lysozyme.

Present experimental observation and past literature has indicated a 30 kD molecular weight impurity with a strong affinity for lysozyme. Literature identifies this protein, present in hen egg white, to be ovomucoid. Based only on physical characteristics such as source and molecular weight, ovomucoid is a possible candidate for the contaminant observed in our stocks. To better understand the persistent affinity this 30 kD molecular weight impurity has for lysozyme, positive identification is presently underway.

### *3. Modeling of diffusive-convective transport and interaction with interface kinetics*

In the previous Progress Reports, we presented a detailed description of our lysozyme crystal growth model and numerical approach. We also provided the first results from our simulations. Since then, these have been submitted and accepted for publication in the Journal of Crystal Growth. We showed that the assumption of fixed crystal size is reasonable for the description of the time-dependent concentration distributions around a growing crystal. Under both purely diffusive and convective-diffusive transport conditions, we obtained significant nonuniformities in interfacial supersaturation, that can reach 20% between the center and the edge of a facet. The simple interface kinetics model used in these simulations assumes that the growth rate is proportional to the *local* supersaturation. Thus, the growth rate should be nonuniform over the facet. Figures 1a-c depict the distribution of the supersaturation $\sigma = \ln (\rho^{int}/\rho^{eq})$ over the interface, the corresponding growth rate, and interface shape, respectively.

On the other hand, our experimental investigations (see Appendix) showed that, in spite of these solute nonuniformities, a macroscopically planar shape is retained during growth. The discrepancy between the experimental observations and those first calculations is due to the fact that the model does not take into account the *microscopic* morphology response to the nonuniform supersaturation. We have now addressed this issue by employing a new interface kinetics model that allows for a variation in step density (proportional to local slope p) and, thus compensates for the supersaturation nonuniformity. The experimental and theoretical support for this growth model are described in details in the Appendix. Here we will only describe the specific assumptions used in the calculation scheme.

We assumed that step generation takes place only at the facet edge, as in most of the experimental cases. Since the rate of step generation typically depends on supersaturation for both dislocation and 2D nucleation generated steps, we assumed that the local slope at the edge

$p_e$ is proportional to the local supersaturation. As shown in a test run and also seen from the experimental data, reversing these two assumptions only slightly changes the numerical results.

*1. Step kinetics without step interaction.* As a first approximation, we assumed the local tangential step velocity v to be a function of only the local supersaturation $\sigma$,

$$v = b^{step}\,\sigma, \tag{1}$$

where $b^{step}$ is a kinetic coefficient. Since $\sigma$ decreases towards the facet center, v must decrease too. To calculate the resulting distribution of p, we started the calculation with uniform slope equal to the initial slope at the facet edge, $p_e$. The interstep distance d was calculated as h/p, where h is the step height, ~100 Å for the (110) lysozyme face. As the steps move against the supersaturation gradient, the distance between steps decreases since leading steps move slower than trailing ones. From the interstep distance, we calculated the local slope p for each point of the grid. Note that the grid used for bulk transport calculations, with 21 grid points across the interface, is too coarse for realistic description of the microscopic interface morphology. Hence, we have used a scheme corresponding to several hundred steps. However, for the calculation of the pdistribution, we linearly interpolated$\sigma$ between the 21 grid points.

The lysozyme concentration at the interface, thus calculated, was used to determine the supersaturation distribution, which was used for the next time step of the calculation. Next, the normal face growth rate R was determined for each point as the product R = p v. This R was used in the boundary condition for the bulk transport part of the simulation. All other characteristics of the bulk transport model were unchanged. So far, we have performed simulations with diffusive transport only. Since our previous calculations involving convection resulted in similar interfacial supersaturation distributions, we do not expect drastic changes on inclusion of convection in the coupled transport-interface kinetics model.

Figure 2 presents the resulting $\sigma(x)$ and R(x) distributions, the interface profile z(x) and the local slope p(x). One sees that even the simplest linear assumption for the $v(\sigma)$ dependence in the form of Eq. (1) resulted in uniform R over the facet. Thus, the face grows parallel to itself and the macroscopically planar interface shape is retained.

*2. Step kinetics with step field overlap.* Figure 2d shows that the local vicinal slope at the facet center, $p_c$, is only ~20 % higher than at the facet edge. This is only natural, since with v proportional to $\sigma$, it is only ~20% slower at the center and thus this small increase in p is sufficient to keep R uniform. However, in our experiments we have observed slope ratios $p_e/p_c$ of up to 0.25. In the Appendix, we have demonstrated that this discrepancy can be explained if we assume (surface diffusion) overlap of the step nutrition fields. We have also provided

independent experimental evidence that such interstep interaction is present in our system. In this case, the tangential step velocity depends on the local supersaturation *and* local slope as

$$v = \frac{b^{step}\sigma}{1+kp}, \qquad (2)$$

where $b^{step}$ is an effective step kinetic coefficient and $k\,p$ is a Peclet number characterizing the relative importance for step motion of serial bulk/surface diffusion and incorporation into steps from the surface. Based on the experimental results requiring k p = O(1), with p typically = $O(10^{-3})$, we chose k = 3000 to obtain growth shapes comparable to the experimental ones in short calculation times.

For the calculation of p and R and the coupled lysozyme concentration, we applied the algorithm described above, using the $v(\sigma)$ dependence of Eq. (2). The $\sigma(x)$, R(x), z(x) and p(x) dependencies obtained for this case are shown in Fig. 3. We see that the growth rate is uniform over the interface, and that after only 2 hours of growth, the calculated interface shape corresponds to the experimentally observed one (Fig. 3, Appendix): the slope at the facet center is ~4 times higher than at the edge.

*3. Impurity effects on step kinetics.* In the Appendix, we show that in the presence of impurities with MW ≈ 40,000, 50,000 and 75,000, the interface attains a concave shape, the local slope is lower at the facet center than at the edges. With the simulations, we aimed to quantitatively show that transport of the higher MW molecules through the solution will lead to their interface nonuniformity and how it can affect microscopic growth kinetics.

Since diffusivities are inversely proportional to molecule size, we assumed that the diffusivity of the foreign species is half of that of lysozyme. To emphasize impurity effects in the model, we assumed that they constitute 10 mole % of lysozyme. This is higher than is suggested by the gel electrophoresis results (Fig. 2 in Appendix). Calculations with lower impurity concentrations $\rho_i$ (results not shown) have demonstrated that the impurity-induced changes in the simulation results are not substantial.

In addition we assumed that the surface concentration $\rho_{i,s}$ of the impurities adsorbed on the facet is proportional to their bulk concentration at the interface. This corresponds to the linear part of a Langmuir adsorption isotherm for low adsorbate concentrations. To calculate the impurity incorporation rate into the crystal and, hence, the impurity flux towards the interface, we considered the adsorbed impurities to be buried into the crystal when a growth layer passes, with a frequency = h/R. Thus, the interface boundary condition for the impurity becomes $D_2\nabla\rho_i = \zeta\,\rho_i\,R$. For the adsorption coefficient (ratio of surface to bulk concentration) we chose

$\zeta = 50$. As the change in lysozyme density with crystallization $(\rho_{cryst}/\rho_{sol})^{lys} = 16$, this value ensures higher impurity to lysozyme ratio in the crystal than in the solution.

Next, based on the experimental observations, we assumed that only the foreign adspecies on the steps affect step propagation. Since $b^{step}$ is typically inversely proportional to the distance between *free* kinks along the step, we obtain

$$v = \frac{b^{step}}{1+\xi\rho_i}\frac{\sigma}{1+kp} \quad . \tag{3}$$

In (3), $\xi$ is a phenomenological coefficient describing impurity action on step motion. In our experiments, the presence of impurities did not strongly lower the normal growth rate. Hence, we assume that $\xi = 0.25$. This value ensures that R is approximately the same as in the pure cases.

Using (3), we determined the impurity-modified p and R distribution for the above case. The resulting $\sigma(x)$, R(x), z(x) and p(x) are shown in Fig. 4. We see that the growth rate is again uniform over the interface. However, after only 3 hours of growth, the calculated interface shape roughly corresponds to the experimentally observed one (Fig. 5, Appendix): the slope at the facet center is ~3 times *lower* than at the edge.

Future work will include natural convection into the model, to possibly explain oscillatory growth rates observed in our experiments.

### *4. Light scattering studies*

The goal of our light scattering studies is to investigate the nucleation behavior of protein solutions for different precipitants. Our recent experiments reveal the power of simultaneous static and dynamic light scattering in measuring precipitant effects on solution-protein interactions and protein hydration. They also contradict aggregation models of protein crystallization.

The protein studied is lysozyme at pH=4.7 in sodium acetate (NaAc) buffer. We have looked at two precipitants: aqueous NaCl-solutions with 50mM sodium acetate (NaAc) as buffer, or plain NaAc buffer of ionic strength comparable to the NaCl solution. In a typical experimental series, we fix the ionic strength of the precipitants and vary the concentration c of lysozyme $2.5 \leq c \leq 70$ mg/ml. The solutions are filtered (.22μm) and centrifuged before measurement (for supersaturated solutions we prepare a separate salt and protein solution and mix them as the last step before measurement).

Light scattering data are aquired with a Brookhaven Instruments 2030AT correlator with 136 channels, and we measure at $\lambda = 514.5$ nm with P = 80mW input power in vv-polarization. For the static measurements we use toluene as scattering standard with $R_{vv} = 24.4*10^{-5}$ cm$^{-1}$.

Both static and dynamic data are collected for 10 different angles between 30-120°, with a typical measurement time of 2 min/angle. Besides contributions from glare at the two most forward angles no angular variation is noticable in either the static or dynamic data. This remains true even in supersaturated solutions, as long as the measurements are completed before the onset of nucleation.

Rayleigh ratios R are determined without subtracting the background signal from the buffer/salt solution. The resulting error is noticeable at the lowest protein concentration but otherwise negligible. In Figs. 5 and 6, we have plotted Kc/R *vs.* c for the two different precipitants. Here K is the instrument constant

$$K = \frac{4\pi^2 n_0^2}{N_A \lambda^4}\left(\frac{dn}{dc}\right)^2 = 8.53x10^{-7}\, cm^2 mol / g^2 \qquad (1)$$

with $n_0$ the refractive index of the solution without the protein, $\lambda$ the wavelength of the incident laser light, and dn/dc = 0.227 ml/g the refractive index increment of lysozyme at $\lambda$=514.5 nm (dn/dc was interpolated from values at $\lambda$=589nm [1] and $\lambda$=488nm [2]). As the lack of angular variation indicates, we are measuring in the S(q=0) limit, where S(q) is the static structure factor of the solution. Therefore we can apply Debye's fluctuation theory and relate the measured intensities to the osmotic pressure $\pi$ (or, equivalently, to the chemical potential $\mu$) of the solution in the form

$$\frac{Kc}{R} = \frac{1}{N_A k_B T}\left(\frac{\partial \pi}{\partial c}\right) \cong \frac{1}{M} + 2B_2 c, \qquad (2)$$

where the last equality is the first order virial expansion of the osmotic pressure and $B_2$ is the second virial coefficient. Both precipitant systems follow the linear behavior indicated by the expansion in eqn. (2). This excludes equilibrium aggregation as contribution factor to the scattering intensity, since it would result in nonlinear behavior in our Kc/R-plots. Neither can aggregation account for the positive slopes of Kc/R at low salt concentrations. We therefore proceeded to analyze our data within the framework of the interaction model. The molecular weight we extract at c = 0 is about 14 000 Dalton and compares well to the accepted value of 14 300 Dalton. The virial coefficents $B_2$ of the solution were extracted from the slope of the Kc/R data. Positive values imply net repulsive interactions, negative values net attractive interactions. For increasing ionic strength the system changes from net repulsive to net attractive interactions. $B_2$ values of numerous protein solutions were measured by Wilson et al. [3]. Comparison with reported crystallization conditions revealed that crystallizing systems were characterized by negative virial coefficient $B_2$ in the range of - 2-10x$10^{-5}$ mol ml/$g^2$. Our $B_2$ values in NaCl are comparable to these results. The persistent linearity of our data well above saturation confirm the validity of the lowest order virial expansion even at the much higher concentrations of supersaturated solutions. Notice that, at the same ionic strength, NaCl reduces

the repulsive interactions more effectively than NaAc. This is consistent with its higher effectiveness as crystallization agent.

Our dynamic scattering results corresponding to the above static measurements are shown in Figs. 7 and 8. The diffusion coefficient D at each concentration is averaged over the 10 measurement angles. At each angle, we perform a single-exponential fit to the correlation data. A more careful second-order cumulant analysis produced typical polydispersities $\delta < 0.03$. The error in D introduced by our single-exponential fit is therefore small; a more detailed polydispersity-analysis is in progress. Similar to our static measurements the diffusivity / polydispersity remains time-independent prior to nucleation. Nucleation itself is charaterized through a time-dependent decrease in diffusivity/ increase in polydispersities with pronounced angular dependencies of both quantities. The values obtained for these conditions are therefore not meaningful other than to indicate, when to disregard a specific measurement from our analysis of time-independent solution behavior.

The general expression for the diffusion coefficient equivalent to the first part of eqn. (2) is [4]

$$D = \frac{M}{N_A f}\left(\frac{\partial \pi}{\partial c}\right)(1-\phi), \tag{3}$$

where $\phi$ is the volume fraction of protein, $f = 6\pi\,\eta(c)\,r_h$ the Stokes friction factor, with $r_h$ the protein's hydrodynamic radius, and $\eta(c)$ the concentration dependent viscosity. Even at the highest concentration, $\phi$ never exceeds 0.05, so the last term in eqn. (3) is negligible. Overall, the diffusion coefficient D is seen to change nonlinearly with c at low as well as high ionic strength and for both types of precipitants. Only at intermediate ionic strength do we observe behavior that might be described with a linear expansion, as used in eqn. (2). Comparable behavior has been observed in a variety of proteins and other systems like micelles and polymer solutions[5]. At fixed protein concentration and for increasing ionic strength, similar to our static results, D decreases more rapidly in NaCl than NaAc. Notice also the pronounced shift in the D(c=0) value in NaAc-solutions, which is absent for NaCl. This will be further discussed in connections with the hydrodynamic radii.

Previous measurements of the solution viscosity $\eta(c)$ indicate linear behavior of this quantity with protein concentration [1]. Combining eqn. (2) and (3) we can eliminate the contributions from interactions (static results) and viscosity to the diffusivity values. We obtain the hydrodynamic radius of the particles in the form

$$r_h = \frac{M k_B T}{6\pi}\frac{Kc}{RD\eta(c)}. \tag{4}$$

This is the generalized version of the Stokes-Einstein relation, accounting for interaction and viscosity effects through the group of three measured quantities Hc/R, D and $\eta(c)$. The resulting

$r_h$-values are plotted in Figs. 9 and 10. The noticeable changes in $r_h$ can not be due to equilibrium aggregation of n-mers, which would require *nonlinear* changes in the Kc/R plots. A preliminary polydispersity analysis revealed no signs of aggregation, either. We therefore interpret the variation in $r_h$ as caused by hydration changes of the individual monomer and not as aggregation of monomers to n-mers. The effects is particularly pronounced in the NaAc-solutions. There is an overall increase in hydration even at very low protein concentrations whenincreasing NaAc-concentration. This behavior is a consequence of the D(c=0) drift in NaAc solutions mentioned before. We have no explanation for this behavior at this point. The hydration data for NaCl are less instructive since the solutions nucleated at much lower ionic. The presence of these nuclei masked the hydration changes. It appear, however, that NaCl decreased hydration of lysozyme much more effectively than NaAc.

In summary, our combined static and dynamic light scattering studies provide a powerful tool in monitoring both the interaction strength of protein solutions via the virial coefficient and the hydration behavior via the dynamic data - when properly accounting for the contributions from interactions and viscosity on the diffusivity. While we can not derive general rules from the observations of a single protein in two precipitants , we are encouraged by the wealth of information contained in our data.

We are expanding our measurements in two directions. We will use several new precipitants, especially ammonium sulfate, which is known to induce precipitation instead of crystallization in lysozyme. Measurements of the corresponding solubilities and viscosities of these solutions are planned. Furthermore, we are trying to connect our results to thermodynamic models of salting out behavior. This work, together with an expanded polydispersity analysis, is in progress.

**References**

[1] W.J Fredericks, M.C. Hammonds, S.B Howard and F. Rosenberger, J. Crystal Growth **141** (1994) 183

[2] B. Guo and W.W. Wilson, private communication

[3] A. George and W.W. Wilson, Acta Cryst. D **50** (1994) 361

[4] V.A. Bloomfield, in " *Dynamic Light Scattering. Applications of Photon Correlation Spectroscopy*"^, ed. by R. Pecora, Plenum Press (New York, 1985), p. 374

[5] J.L. Wu, Y.M. Wang, M. Hara, M. Granville and R.J. Jerome,Macromolecules **27** (1994) 1195; M.B. Weissman, R.C. Pan, and B.R. Ware, J. Chem. Phys. **70** (1979) 2897; T. Raj and W.H. Flygare, Biochemistry **13** (1974) 3336; W. Brown and P. Zhou, Macromolecules **24** (1991) 5151

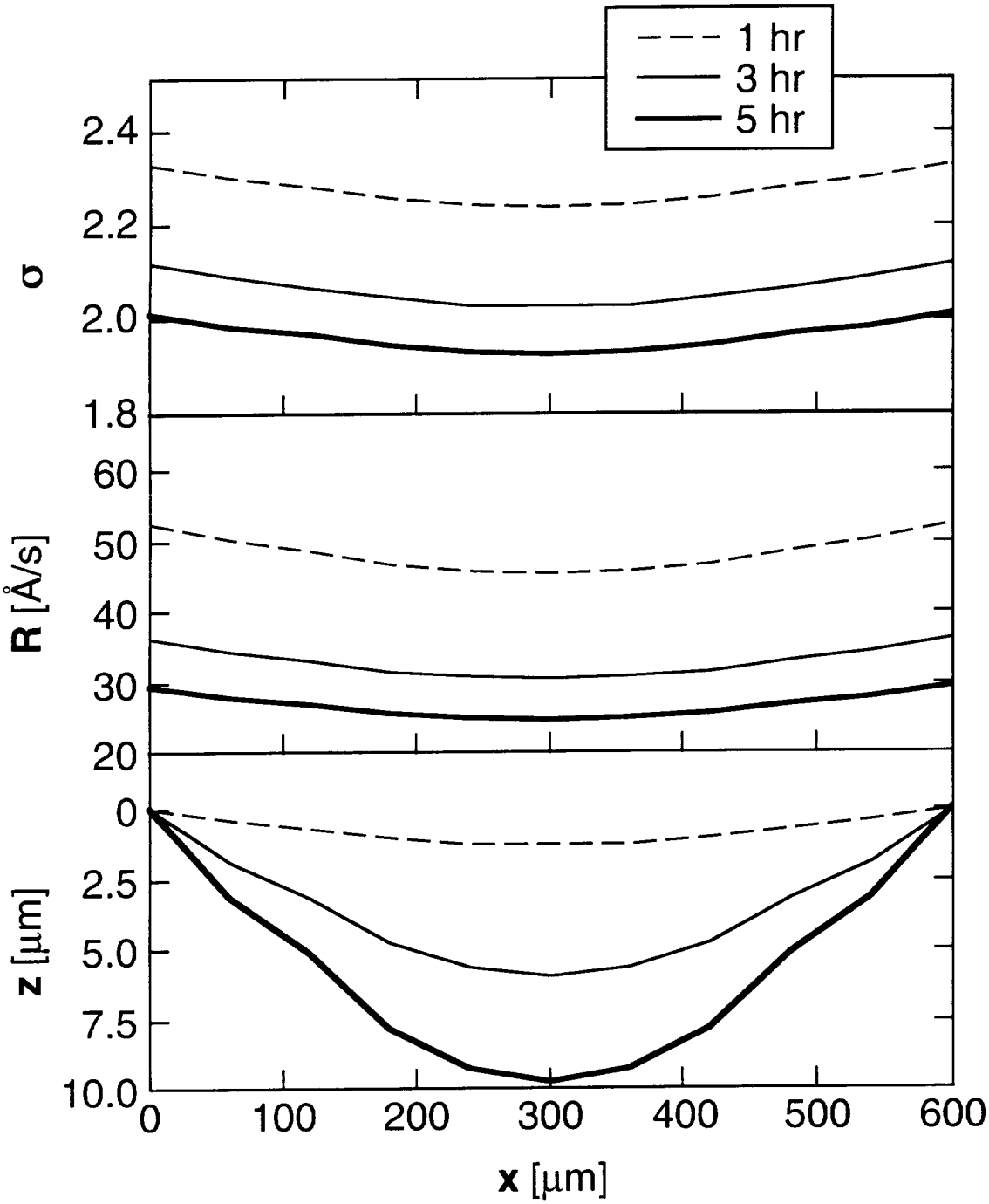
1 hr
3 hr
5 hr
σ
2.4
2.2
2.0
1.8
R [Å/s]
60
50
40
30
20
z [μm]
0
2.5
5.0
7.5
10.0
0
100
200
300
400
500
600
x [μm]

FIG. 1

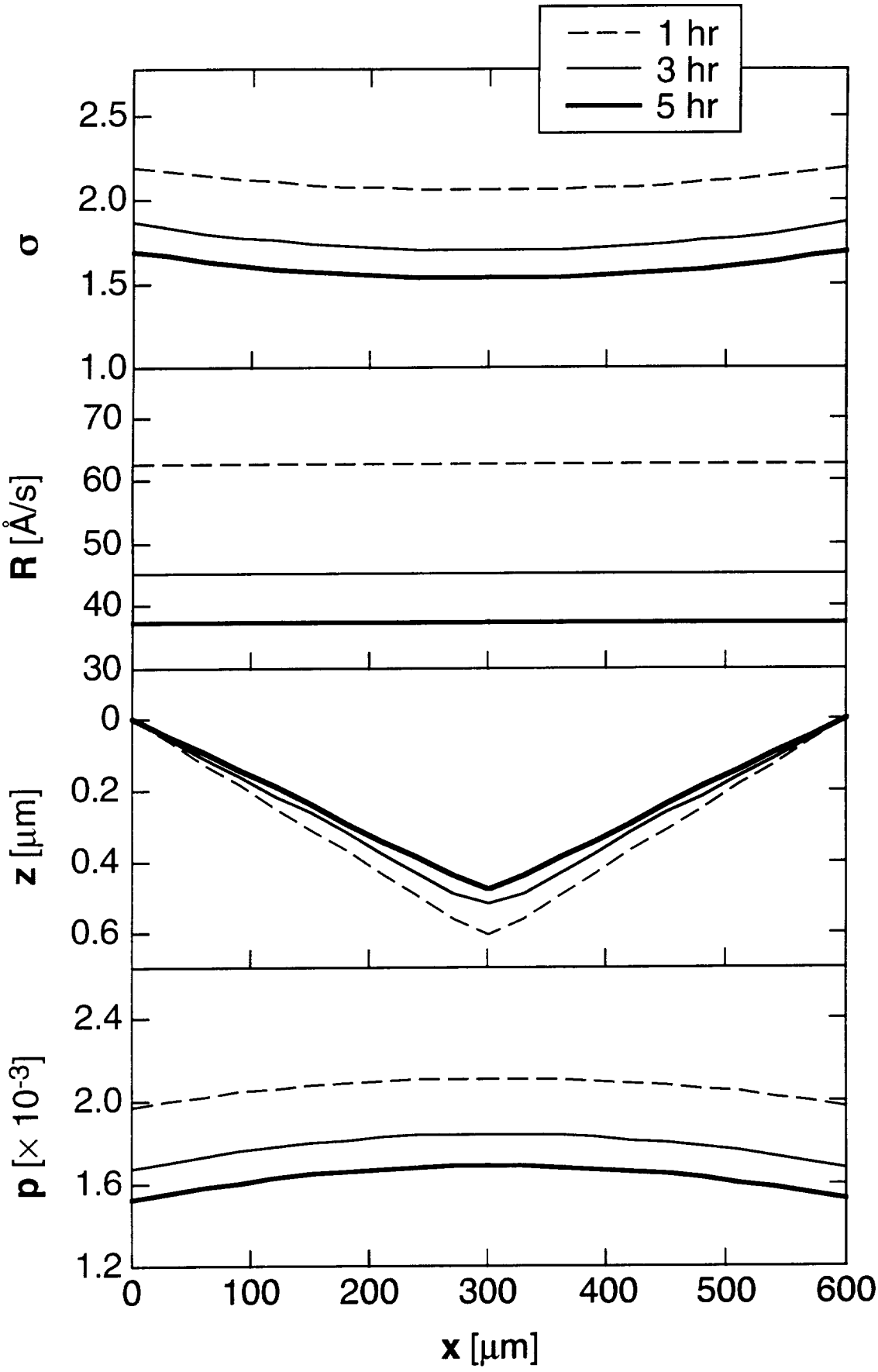
1 hr
3 hr
5 hr
σ
2.5
2.0
1.5
1.0
R [Å/s]
70
60
50
40
30
z [μm]
0
0.2
0.4
0.6
p [× 10-3]
2.4
2.0
1.6
1.2
0
100
200
300
400
500
600
x [μm]

FIG. 2

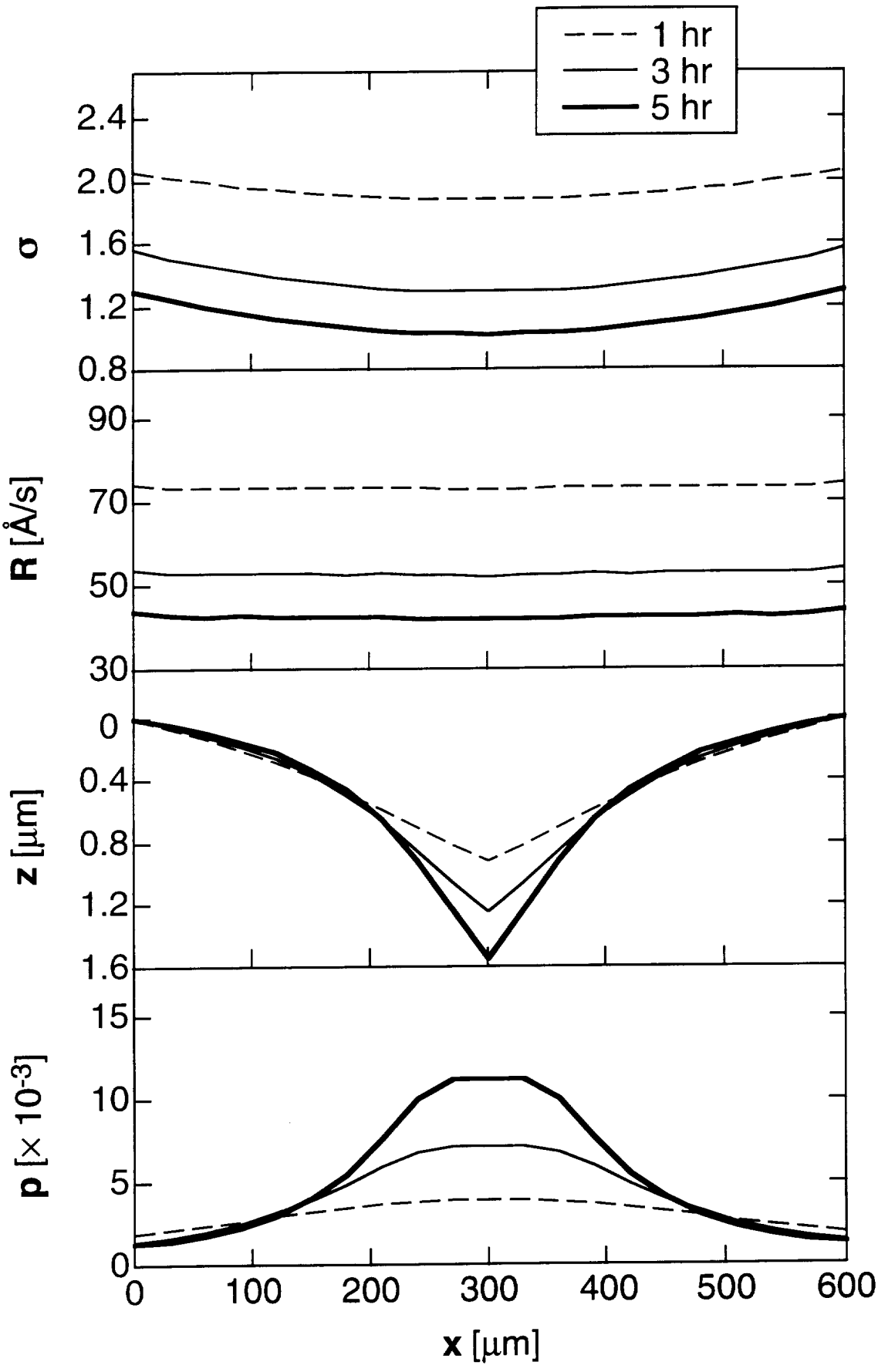
1 hr
3 hr
5 hr
σ
2.4
2.0
1.6
1.2
0.8
R [Å/s]
90
70
50
30
z [μm]
0
0.4
0.8
1.2
1.6
p [× 10-3]
15
10
5
0
0
100
200
300
400
500
600
x [μm]

FIG. 3

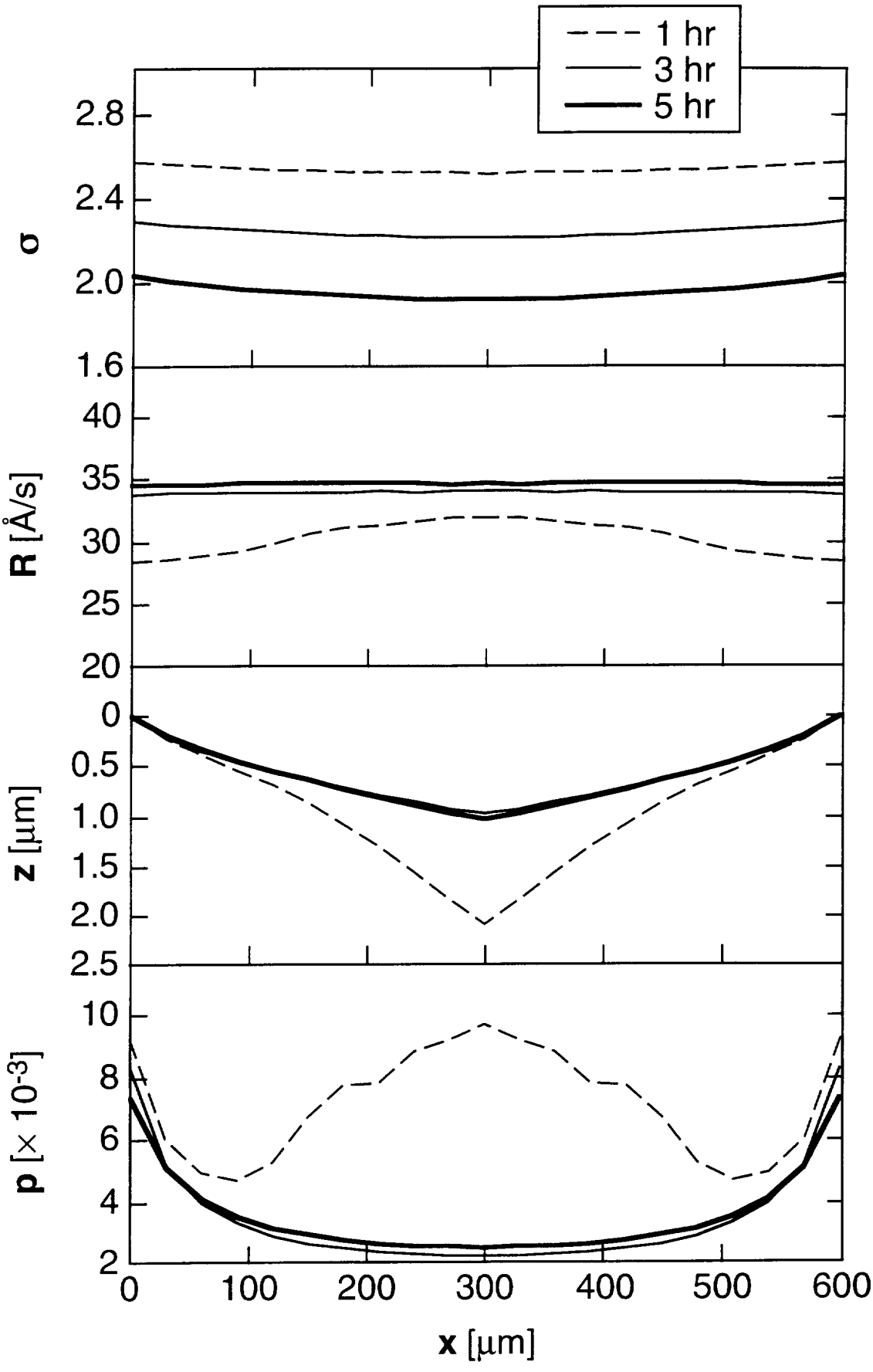
1 hr
3 hr
5 hr
σ
2.8
2.4
2.0
1.6
R [Å/s]
40
35
30
25
20
z [μm]
0
0.5
1.0
1.5
2.0
2.5
p [× 10-3]
10
8
6
4
2
0
100
200
300
400
500
600
x [μm]

FIG. 4

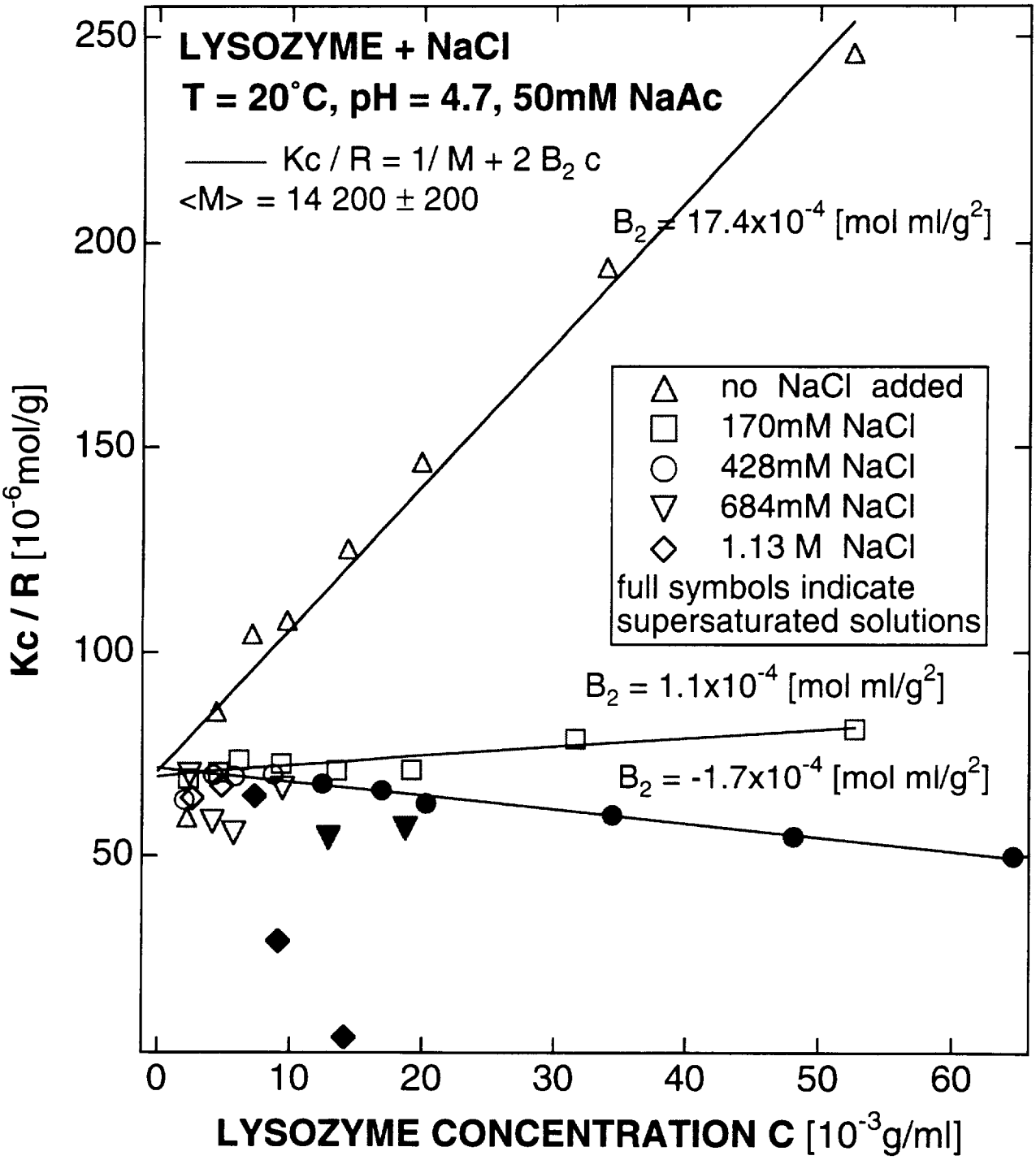
LYSOZYME + NaCl
T = 20°C, pH = 4.7, 50mM NaAc
Kc / R = 1/ M + 2 B2 c
<M> = 14 200 ± 200
B2 = 17.4x10-4 [mol ml/g2]
B2 = 1.1x10-4 [mol ml/g2]
B2 = -1.7x10-4 [mol ml/g2]
no NaCl added
170mM NaCl
428mM NaCl
684mM NaCl
1.13 M NaCl
full symbols indicate supersaturated solutions
Kc / R [10-6mol/g]
LYSOZYME CONCENTRATION C [10-3g/ml]
250
200
150
100
50
0
10
20
30
40
50
60

FIG. 5

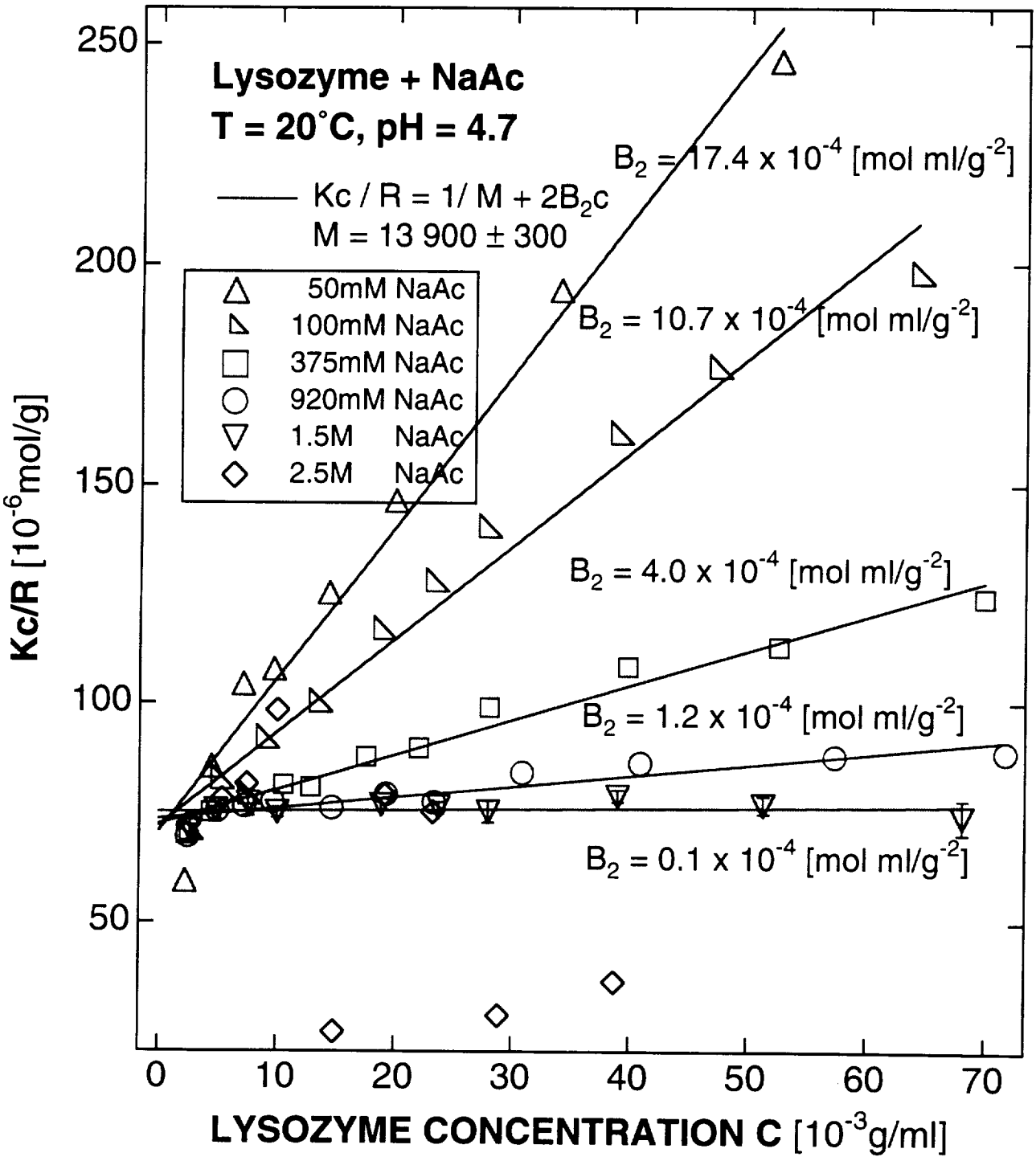
Lysozyme + NaAc
T = 20°C, pH = 4.7
Kc / R = 1/ M + 2B2c
M = 13 900 ± 300
50mM NaAc
100mM NaAc
375mM NaAc
920mM NaAc
1.5M NaAc
2.5M NaAc
B2 = 17.4 x 10-4 [mol ml/g-2]
B2 = 10.7 x 10-4 [mol ml/g-2]
B2 = 4.0 x 10-4 [mol ml/g-2]
B2 = 1.2 x 10-4 [mol ml/g-2]
B2 = 0.1 x 10-4 [mol ml/g-2]
Kc/R [10-6mol/g]
LYSOZYME CONCENTRATION C [10-3g/ml]
250
200
150
100
50
0
10
20
30
40
50
60
70

FIG. 6

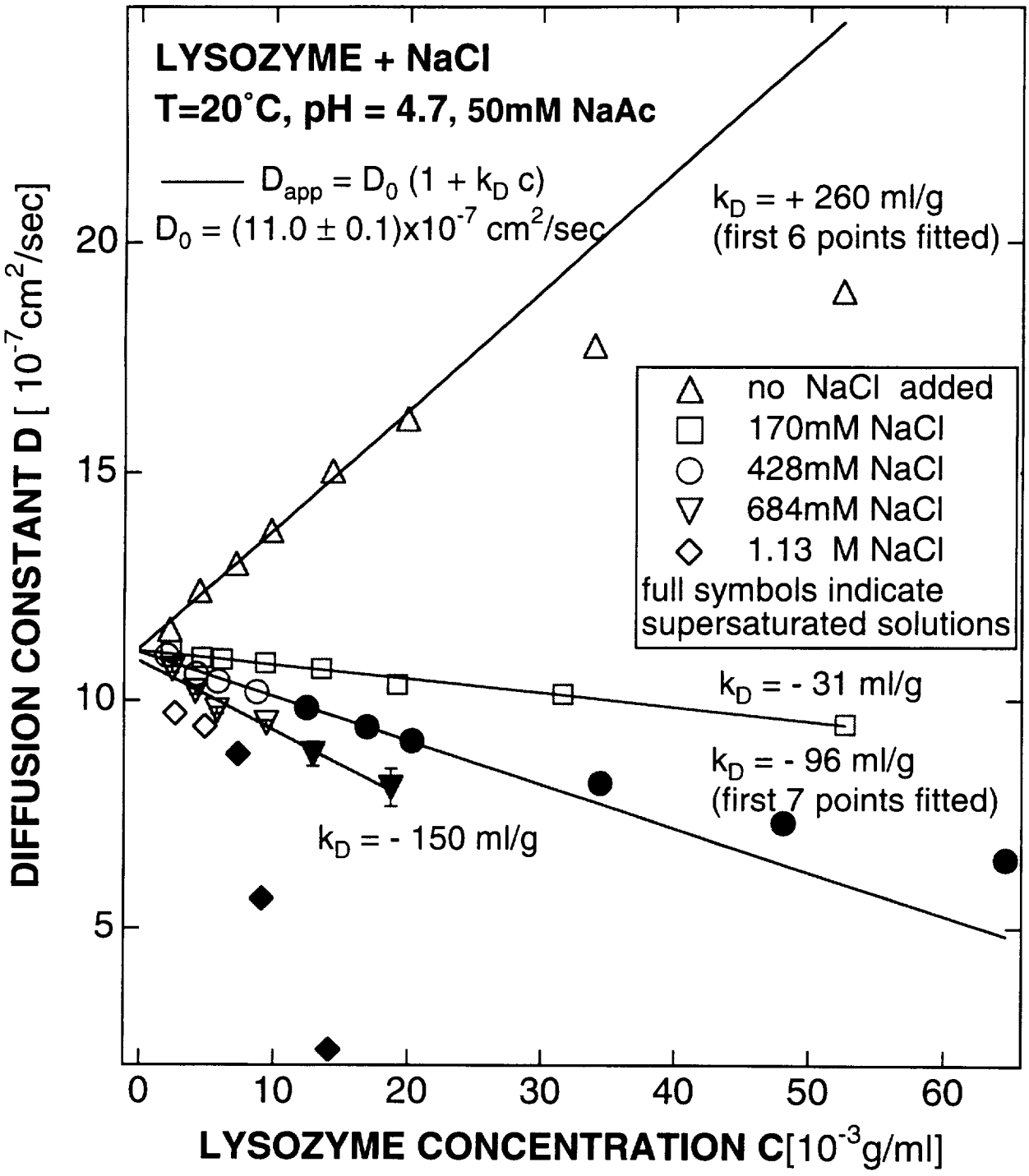
LYSOZYME + NaCl
T=20°C, pH = 4.7, 50mM NaAc
$D_{app} = D_0 (1 + k_D c)$
$D_0 = (11.0 \pm 0.1) \times 10^{-7}$ cm²/sec
$k_D$ = + 260 ml/g
(first 6 points fitted)
no NaCl added
170mM NaCl
428mM NaCl
684mM NaCl
1.13 M NaCl
full symbols indicate supersaturated solutions
$k_D$ = - 31 ml/g
$k_D$ = - 96 ml/g
(first 7 points fitted)
$k_D$ = - 150 ml/g
DIFFUSION CONSTANT D [ $10^{-7}$cm²/sec]
LYSOZYME CONCENTRATION C[$10^{-3}$g/ml]
0
10
20
30
40
50
60
5
10
15
20

FIG. 7

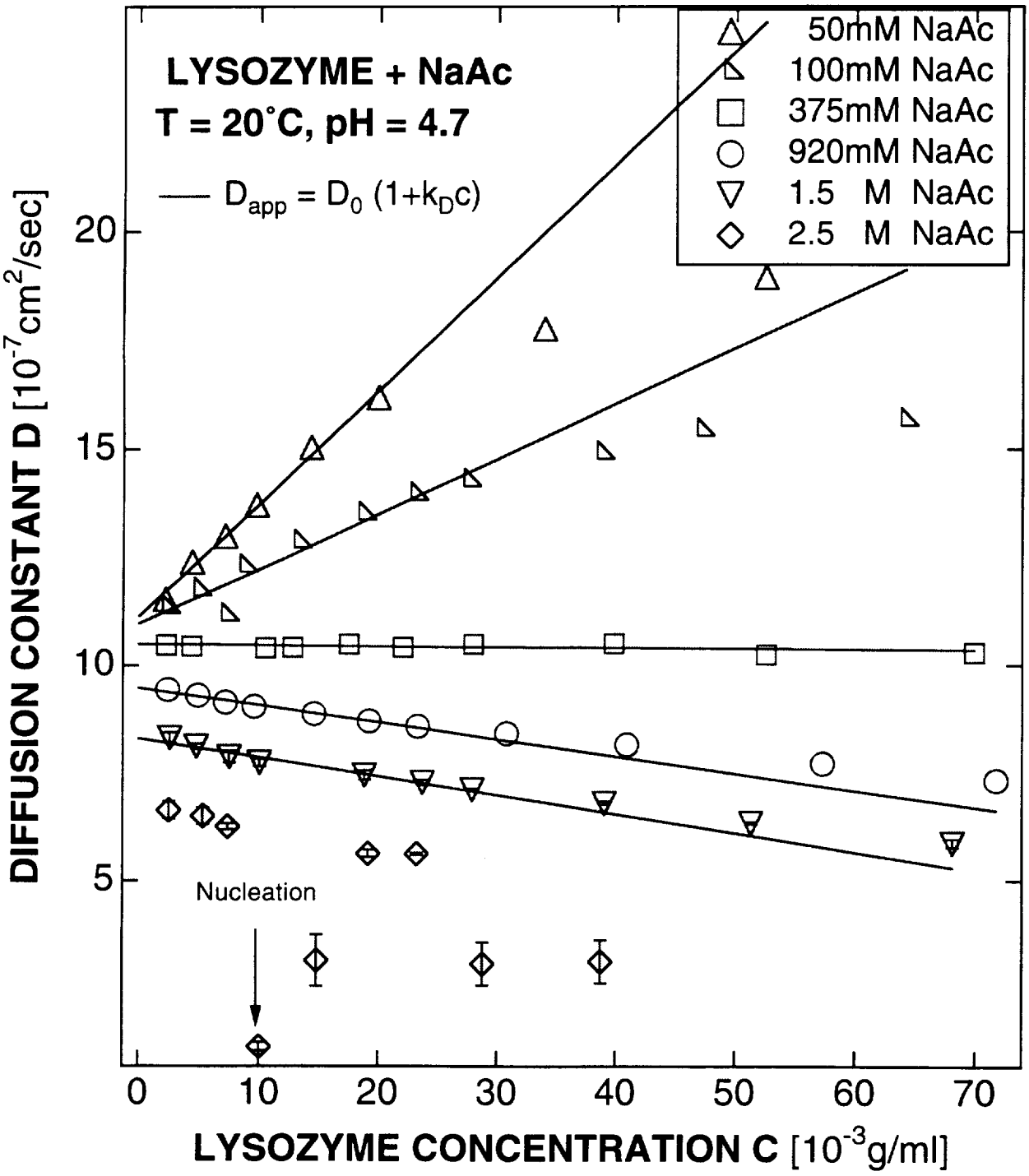
LYSOZYME + NaAc
T = 20°C, pH = 4.7
$D_{app} = D_0 (1+k_D c)$
50mM NaAc
100mM NaAc
375mM NaAc
920mM NaAc
1.5 M NaAc
2.5 M NaAc
Nucleation
DIFFUSION CONSTANT D [$10^{-7}$cm$^2$/sec]
LYSOZYME CONCENTRATION C [$10^{-3}$g/ml]
0
10
20
30
40
50
60
70
5
10
15
20

FIG. 8

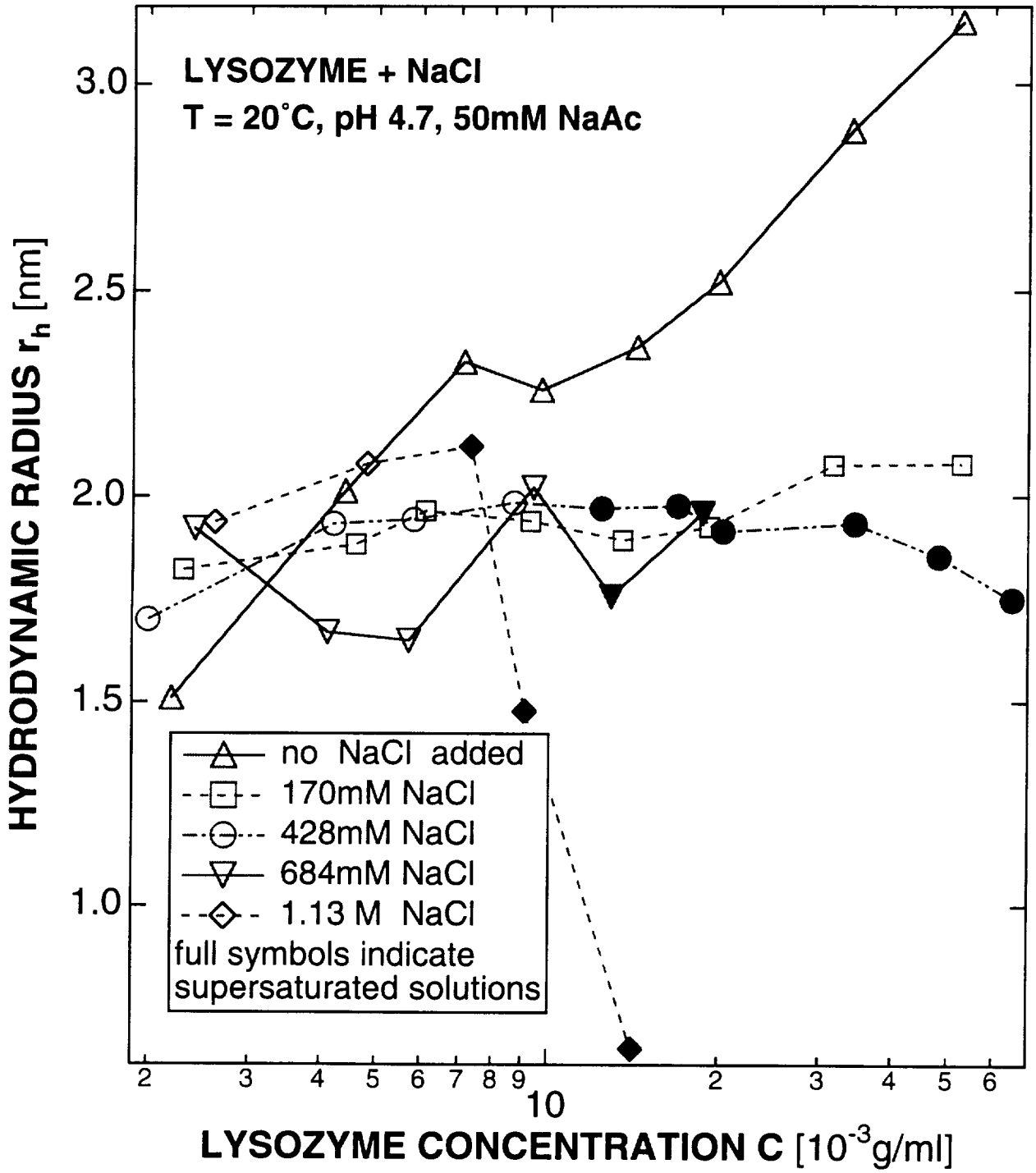
LYSOZYME + NaCl
T = 20°C, pH 4.7, 50mM NaAc
HYDRODYNAMIC RADIUS $r_h$ [nm]
3.0
2.5
2.0
1.5
1.0
no NaCl added
170mM NaCl
428mM NaCl
684mM NaCl
1.13 M NaCl
full symbols indicate supersaturated solutions
2 3 4 5 6 7 8 9 10 2 3 4 5 6
LYSOZYME CONCENTRATION C [$10^{-3}$g/ml]

FIG. 9

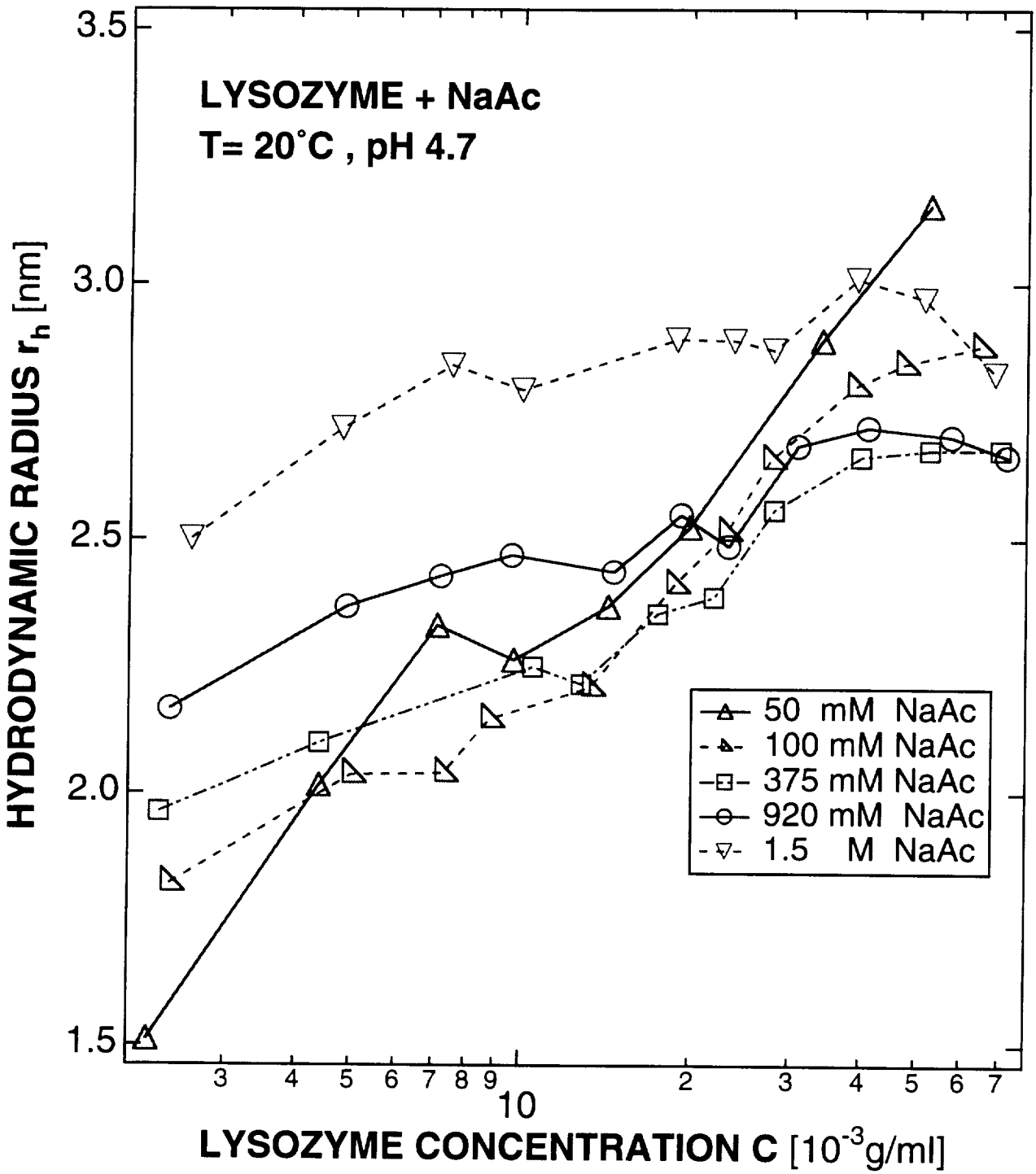
LYSOZYME + NaAc
T= 20°C , pH 4.7
HYDRODYNAMIC RADIUS $r_h$ [nm]
3.5
3.0
2.5
2.0
1.5
3 4 5 6 7 8 9
10
2 3 4 5 6 7
LYSOZYME CONCENTRATION C [$10^{-3}$g/ml]
50 mM NaAc
100 mM NaAc
375 mM NaAc
920 mM NaAc
1.5 M NaAc

FIG. 10

# Growth morphology response to nutrient and impurity nonuniformities.

# I. Experimental observations and theoretical interpretation

Peter G. Vekilov, Lisa A. Monaco and Franz Rosenberger

*Center for Microgravity and Materials Research,*

*University of Alabama in Huntsville, Huntsville, AL 35899, USA*

## Abstract

The growth morphology and kinetics on facets of tetragonal lysozyme crystals was investigated by in-situ high-resolution optical interferometry. The protein composition of the growth solutions was characterized by gel electrophoresis and high pressure liquid chromatography. In solutions that contained only one protein impurity (molecular weight MW ≈ 30,000), the facets were microscopically convex, that is with higher vicinal slope in the center than at the edge. In solutions containing less than 1 % of higher MW impurities that are incorporated into the crystals, the facets were microscopically concave, with lower slope at the center than at the edge. Both deviations from planarity increased with crystal size and growth rate. This indicates that these morphologies are caused by nonuniformities in interfacial nutrient and impurity concentrations. Quantitative accounts of both interface shapes are possible only if one assumes strong overlap of the coupled volume and surface diffusion fields of growth steps. This indicates that the characteristic surface diffusion length of admolecules on lysozyme {110} facets is of order 1 μm or ~100 unit cell lengths. Tangential velocities measured in the less pure solutions strongly suggest that the impurities affect growth kinetics through adsorption at kink sites.

## 1. Introduction

The nutrient fields around growing polyhedral crystals do not possess the symmetry of the crystal habit. If solute transport is dominated by diffusion, as, for instance, at reduced gravity or in thin growth chambers, the concentration fields tend to attain spherical symmetry (see the classical interferograms by Humphreys-Owen [1], and various model calculations [2-5]). Thus,

nutrient concentrations at edges and corners of growing crystals are generally higher than at facet centers. The resulting growth rate nonuniformity must lead to some loss of facet flatness such that facets are depressed in the center. However, in many cases *macroscopic* flatness of the crystal faces is retained. This morphological stability of a polyhedral crystal in a nonuniform supply field has been dealt with extensively [6-15]. Macroscopic flatness can be retained through compensating changes in the local kinetic parameters associated with the changes in the *microscopic* morphology that forms *in response* to the solute nonuniformities.

Similar to the transport of solute, impurities that are (partly) incorporated into a crystal, are more readily replenished from the bulk solution to crystal edges and corners. Again, if such impurities influence the growth kinetics, the resulting growth rate nonuniformity must result in some deviation from planarity. Such effects have been investigated to a much lesser extent [15,16].

For a facet to remain macroscopically flat, its normal growth rate R must be uniform. For layer growth that is limited only by incorporation processes at the steps, the (local) R can be written as [17]

$$R = p\, v = p\, \beta_{step}\, \Omega\, C\, \sigma \ , \qquad (1)$$

where p is the vicinal slope (proportional to the locally averaged step density), v the tangential (average step) velocity, $\beta_{step}$ the step kinetic coefficient, $\Omega$ the (molar) volume of the solute in the crystal, C the interfacial solution (molar) concentration, and $\sigma$ the interfacial supersaturation. Hence, R can be uniform only if nonuniformities in interfacial solute field or in $\beta_{step}$ (from impurity transport) are compensated by nonuniformities in local step density. For instance, in a facet's center region, in spite of the lower local $\sigma$, R may retain essentially the same value as at the edge, because of the steeper slope that forms in the center in response to the leaner supply.

Fig. 1a schematically illustrates, for a system with (dominant) step generation at the facet edge, the mechanism of microscopic shape response to nonuniform supersaturation. Of a pair of steps advancing towards the facet center in the direction of spatially decreasing $\sigma$, the leading step

moves slower than the trailing step, which is always at higher $\sigma$. Thus, the distance between the steps decreases, causing an increase in vicinal slope, i.e., in local step density.

The earlier studies of the morphological response of facets to nonuniform nutrient supply concerned mostly the conditions resulting in the loss of R uniformity to an extent that depressions in facet centers were macroscopically detectable [15,16,18,19]. Only recently, interferometry investigations [15,20], as well as Monte Carlo simulations of facet morphologies in a diffusive supply field [21-23], confirmed the validity of the theoretically predicted stabilization mechanism on a microscopic level.

Fig. 1b shows, in analogy to Fig. 1a, what microscopic morphology we might expect in response to a nonuniform distribution of impurities that impede the host attachment kinetics. Of a pair of steps advancing towards the facet center, the leading step, in response to the spatially decreasing impurity concentration $C_i$, moves faster than the trailing step that is always at higher $C_i$. Thus, the distance between the steps increases, causing a decrease in vicinal slope and local step density. Such growth shapes have not been observed to date.

In the following we will present an investigation of the microscopic interface shapes of tetragonal lysozyme crystals growing from solutions with different impurity concentrations. In growth from purer solutions, we confirmed that in response to nutrient supply nonuniformities the local vicinal slope is higher at the facet center (convex interface shape). The observed magnitude of this effect strongly suggests that the step diffusion fields overlap in our system. In the presence of higher molecular weight impurities, we found, for the first time, p to be higher at the periphery (concave interface shape). Our results indicate that this shape is the result of the nonuniform supply of step impeding impurities to the interface. Depending on the specific growth conditions, that favor either the intrinsic or impurity mechanism, or their compensation, we observed either concave, convex or uniformly sloped interface shapes in growth from the same solution.

The experimental setup and procedures, and the data collection and processing routines were as described earlier [24]. In all experiments the solutions contained C = 50 mg/ml lysozyme and 2.5 % (w/v) NaCl in 0.05 M sodium acetate buffer with pH = 4.5. Supersaturation was

calculated as $\sigma = \ln[C/C_{sat}(T)]$, where $C_{sat}(T)$ is the lysozyme solubility at the growth temperature [25].

## 2. Solution purity characterization

Lysozyme from two sources was used in the growth experiments: Seikagaku Kogyo, and Sigma Chemicals. Lysozyme supplied by Boehringer-Mannheim was used for additional cross-reference in the impurity analyses. The protein composition of initial solutions, and dissolved crystals and supernatants from growth experiments was determined by sodium dodecyl sulfate polyacrylamide gel electrophoresis (SDS PAGE). For this we employed the PhastSystem from Pharmacia LKB using homogenous 12.5% pre-cast gels. Protein distribution along the gel lanes was visualized by silver staining. The lower limit of protein detection by this method is between 1-10 ng [26], which is about 100 times lower than the limit obtainable with commonly used Coomassie blue staining [26]. For lanes loaded with 8 μg lysozyme, this results in a detection limit for other proteins of ~0.1 %. Fig. 2 shows that within this limit, the Seikagaku solutions are the purest of the three. Besides lysozyme with MW ≈ 14,000, one sees only one impurity with MW ≈ 27,000-30,000. This protein is most likely ovomucoid [27,28], whose molecular weight has been reported to vary over this range [27]. The Sigma initial solution contains three other protein impurities with approximate molecular weights of 40,000 and 75,000, presumably ovalbumins and ovotransferrins [28], and an unidentified protein of MW ≈ 50,000 also seen in Ref. [28]. The Boehringer-Mannheim lanes are consistent in Figs. 2a and 2b and indicate somewhat different impurity contents. In other measurements, the concentration of the impurities, as judged from the intensities of the respective bands, varied somewhat. Sometimes, a faint band at MW ≈ 50,000 appeared even in Seikagaku solutions (gels not shown). Note that the SDS PAGE method is sensitive to proteins only; if lysozyme from the three sources contains non-protein impurities, we would not detect them.

To roughly estimate the amount of protein impurities in the Sigma solutions, we ran gels with loads of 1, 5, 10, 20, 40, 60, 100, 500 and 1000 ng lysozyme per lane (not shown). Lysozyme bands were consistently visible in the lanes loaded with ≥ 10 ng protein. Thus the

lower detection limit in our determinations is within the range cited in Ref. [26]. The intensities of the bands of impurities with MW ≈ 40,000, 50,000 and 75,000 in the Sigma solution in Fig. 2b are comparable to the bands in those test runs loaded with 20-60 ng. Assuming that equal masses of different proteins lead to approximately the same intensities of silver stained bands, the impurity contents of these solutions is ~0.5-1 % mass with respect to lysozyme. The contents of the protein with MW ≈ 27,000–30,000 seems to be several times higher in all solutions.

In comparing the lanes for dissolved crystals grown from Sigma lysozyme with their supernatant and initial solution (Fig. 2b), we see that the MW ≈ 75,000 protein is preferentially incorporated into the crystals, while the components with MW ≈ 27,000-30,000 and 50,000 are distributed between crystals and supernatant approximately proportionally to lysozyme contents. The MW ≈ 40,000 protein is predominantly rejected by the crystals.

We have confirmed the higher purity of the Seikagaku lysozyme solutions by ion-exchange and gel filtration high-pressure liquid chromatography. Further evidence is provided by previous kinetics experiments on {101} lysozyme faces [29], as well as our recent studies of nonsteady growth on {110} faces [30]. Both studies have shown that tangential step velocities in the supersaturation range 0.5 to 1.5, from which the kinetic coefficient $\beta_{step}$ is deduced, are several times greater in Seikagaku than in Sigma solutions.

## 3. Experimental results and discussion

### *3.1. Purer solutions*

Fig. 3 illustrates the morphology of a (110) crystal face growing from a Seikagaku solution. The crystal was oriented in such a way that the interference fringes in Fig. 3a are representative of the growth fronts' orientation [24]. One sees that the growth layer generation is dominated by five sources (A-E) along the facet edges and three sources (F-G) in the middle of the facet. This is in contrast to the expectation [29,31] that, at the $\sigma$ = 2.6 employed, steps are uniformly generated over the facet by 2D nucleation [31-33]. Two mechanisms could account for the observed step source localization. Firstly, in analogy to observations on select inorganic crystals [34-39], the locations of preferential nucleation could be associated with higher local

densities and/or activities of outcropping defects. Secondly, the higher $\sigma$'s at the edges need to be considered: In other runs under similar conditions we have observed nucleation to exclusively occur along the edges when the crystals were larger than 100-120 μm (see the later figures, Fig. 8 in Ref. [24], and Ref. [20]). Hence, we interpret the preferential step generation at the edges as a manifestation of higher supersaturation in these regions, see also Ref. [23].

Fig. 3a shows also that the interfringe distance in the [110] directions is about twice that along [001], i.e., that the steps propagate half as fast in the [001] directions. Since this can hardly be interpreted in terms of nutrient supply nonuniformity, we conclude that this anisotropy of surface morphology is due to an anisotropy of the step kinetic coefficient. In analogy to inorganic systems, this $\beta_{step}$ anisotropy could either be intrinsic or impurity-induced [40].

Fig. 3b shows the height profile, calculated as in Ref. [24], along the line indicated in Fig. 3a. One sees that the local vicinal slope, explicitly shown in Fig. 3c, is about 4 times lower at the facet edges than at the facet center. Measurements of the tangential velocity at various locations showed a fourfold decrease of v from edge to center, independent of step propagation direction. This accounts for the R uniformity over the facet. It is important to note that R-, p- and v-values given in this paper represent *averaged values* obtained over periods of order 10 min. The actual, non-steady short-term behavior of this system will be presented in a separate publication [30].

To possibly correlate the convex interface shape with nutrient supply nonuniformities, we followed the evolution of a facet morphology with increasing crystal size, see Fig. 4. The growth rate was monitored at four locations, of which two were also used for slope monitoring (see the x's in Fig. 4). Note that slopes were always determined normal to the fringes at the respective locations; see also Ref. [24]. In general, the concentration nonuniformities increase with both growth rate and crystal size. To distinguish effects due to growth rate from those of crystal size, we alternated between two supersaturations. Although R remained uniform over the face throughout this series, on returning to the same supersaturation at different times, different R's were obtained. Since these changes in R were accompanied by corresponding slope changes at the

step sources, we attribute the R changes, as in inorganic crystals [41], to changes in step source activity.

Comparing Figs. 4a, 4c and 4f, we see that at the same bulk $\sigma$, and roughly the same R and slope at the edge, $p_e$, the slope in the center, $p_c$, increases to 2.5 $p_e$ with ~1.7 fold increase in facet width $a$. This reflects the increasing supply nonuniformity with crystal size [2-4]. Further, in comparing Fig. 4b with 4c, or 4e with 4f, one sees that at similar crystal sizes, $p_c$ increases with increasing R. However, Figs. 4c and 4d show that at a given $\sigma$ and similar crystal size, a reduced R results in a more uniform slope. This observation highlights the importance of the growth rate, as opposed to supersaturation, for interface shape determination. Since for a given crystal size the solute nonuniformity increases with R, this observation particularly well supports our supposition that nonuniformities in the nutrient supply are the cause for the observed interface morphology.

Although the observed convex shape agrees qualitatively with the expected stabilization mechanism through slope variation, the low values of $p_e/p_c$ (0.25 in Fig. 3 !) pose an interesting problem. According to the simple relation for growth limited only by solute incorporation into steps , Eq. (1), such small slope ratios would indicate differences in interfacial supersaturation between center and corner of several hundred percent. However, from our detailed model calculations [5,42], that are based on realistic kinetics and transport parameters for lysozyme, we expect $\Delta\sigma/\sigma$ not to exceed 20%. As we will quantitatively show in Section 4, this apparent discrepancy can be interpreted in terms of overlapping surface diffusion fields of the growth steps [43-45]. Qualitatively, as the step density (slope) increases in response to the lower supersaturation, the steps slow down additionally due to increasing overlap of their nutrient field. This further decreases the distance between them and, thus, increases the slope.

Independent evidence for the overlap of step diffusion fields was deduced from an etching experiment performed with another crystal; for technical details on in-situ etching in our experimental setup see Ref. [20]. Step motion in dissolution is considered symmetrical to that in growth [46,47]. We used a facet that had become flat in response to low supersaturations (and, thus, vanishing solute nonuniformity), see Figs. 4b and 4d. Then we etched the crystal at low

supersaturation such that the etching rate was only R = -1.4 Å/s. The central regions remained flat. This means that the now outward moving steps remain essentially equidistant, which, in turn, indicates the absence of significant interfacial σ-nonuniformities. At the same time, etching steps formed at the edges moved inward. The resulting edge profile had a gradual decrease in slope from $p_{high} \approx 40\times10^{-3}$ (limited by the instrument) to $p_{low} = 6\times10^{-3}$. At the prevailing uniform undersaturation conditions, the slope at the edge would be uniform unless the step generation rate at the edge changes, which is not likely. Hence, it appears that the reason for the spatially decreasing slope is an overlap of the step diffusion fields, see model in Ref. [48].

Further support for the presence of interstep interaction will be given in our report on the non-steady growth kinetics observed in this system [30].

*3.2. Impurity induced interface shape*

Fig. 5 shows the interface morphology of a crystal growing from a Sigma solution, containing higher MW impurities. Contrary to the observation in the purer solution, the average vicinal slope at the facet corner is now about 6 times *higher* than at the facet center. As we have seen in Fig. 2, the proteins with MW≈27,000-30,000, 50,000 and 75,000 are incorporated into the crystals. This creates a flux of impurity species towards the crystal. Since the higher molecular weight impurities have lower diffusivities than lysozyme [49], the nonuniformity in their interfacial concentrations will be more pronounced and its effect may overpower the effect of lysozyme concentration nonuniformity.

To experimentally test whether the concave interface shape is related to nonuniform impurity transport, we followed the surface morphology as a function of crystal size at a fixed supersaturation. Fig. 6 shows that $p_e/p_c$ strongly increased with crystal size. The concave interface shape in the presence of higher MW impurities was also observed during the growth of {101} lysozyme faces. Although the $p_e/p_c$ ratio was lower, it again increased with crystal size, indicating the same mechanism of morphology formation as on {110} faces.

The connection between impurity nonuniformity and concave interface shape is illustrated above in Fig. 1b. If step motion is impeded by impurities, lower impurity concentrations in the

facet center region leads to accelerated step motion as steps advance towards the center. This results in greater interstep distance and lower vicinal slope at the facet center than at the edges. A formal description of this effect is presented in Section 4.

*3.3. Combined effects*

Above we have shown that, depending on impurity content, either concave and convex interfacial morphologies can be obtained. In other observations, with facets possessing different step source distributions and activities, we have obtained both types of growth shapes on the same crystal.

Fig. 7 presents the development of an interface morphology during growth from a Sigma solution. While the facet grew significantly in the direction of view, the lateral crystal dimension remained essentially constant during this sequence. In the first frame, Fig. 7a, growth layer sources are located near the corners A and C of the facet. These sources remained active throughout the entire sequence, and their activity sharply increased at $\sigma = 3.24$, Fig. 7d. In the first frame the growth rate is so low that probably neither impurity nor solute nonuniformities are significant. Consequently, the slope is almost constant over the interface. In Fig. 7b an additional strong growth source appears at corner B. Steps are also generated along the two lower visible edges of the crystal. The slope decreases from the periphery to the center, in accordance with the impurity effects described above.

In Fig. 7c, the edge A-B is no longer active as layer source. The slope of the step train generated at corner B first increases and then decreases in the direction towards the facet center. Apparently, close to corner B, the supersaturation gradient effect is stronger than the impurity effect, resulting in a convex shape. However, closer to the facet center, where the interface profile becomes concave, impurity effects appear to be stronger.

In the same frame, the subtle competition between the impurity and solute effects on step motion is particularly well reflected by the steps moving (on average) from B towards A. Over the first 50 μm from the edge, both the fringe curvature and spacing increase in this direction. This reflects an increase in step velocity with distance from the edge. Thus the effects from impurity

gradients appear to overpower the step deceleration due to the $\sigma$ gradient. Beyond this edge region, both the curvature and fringe spacing decrease to the middle of the facet, as a result of the dominating $\sigma$ nonuniformity. The steps originating in corner C exhibit similar behavior. The reduction of the impurity effects compared to Fig. 7b may reflect either a decrease in impurity concentration with progressing crystallization, or time dependent impurity adsorption [29,50].

With further growth, the impurity effects appear to be still weaker; Fig. 7d. At the higher supersaturation, a step source close to corner A is now dominating the morphology of the left half of the facet, resulting in a reversal of the curvature of the fringes. However, the width of the edge region in which the impurity effects dominate, is considerably reduced.

## 4. Theoretical interpretation of the observed growth shapes

### *4.1. Nonuniform solute distribution effects*

*4.1.1. Direct incorporation into steps with bulk diffusion step field overlap.* As we have seen in Section 3.1, the observed low $p_e/p_c$ values cannot be explained by Eq. (1) that applies to growth via noninteracting steps. This is not surprising in view of the evidence for step field interaction presented above. In order to possibly distinguish between volume and combined volume-surface field overlap, let us first consider the possibility of step interaction through overlapping bulk diffusion fields, still assuming direct incorporation of solute from the solution into steps. For this growth mode, both, BCF's [43] and Chernov's [51] relations for the dependence of step velocity on supersaturation and vicinal slope can be written as

$$v = \frac{\beta_{step}\,\Omega\,C\,\sigma}{1 + (\beta_{step}\,\delta/D)\,p} \quad , \tag{2}$$

where $\delta$ is the thickness of the interfacial solute-depletion layer and D is the bulk diffusion coefficient. For tetragonal lysozyme, $\beta_{step} \approx 3\times10^{-4}$ cm/s [29,30], D = $0.73\times10^{-6}$ $cm^2/s$ (measured for the solution composition used here [52]). In our experiments $p \approx 5\times10^{-3}$ and thus $\delta$ should be ~ 0.5 cm so that $(\beta_{step}\delta/D)p \sim 1$ that could account for the available experimental evidence for step field overlap: the low $p_e/p_c$ ratio, the decreasing slope of the etching profile of the edges and the coupled fluctuations in p and v (see Sect. 3.1.). On the other hand, model

calculations in geometry and conditions representative of the experiment [5] helped us to estimate $\delta \approx 150$ μm. Thus, the hypothesis of overlapping of the bulk diffusion fields followed by direct incorporation into the steps cannot *quantitatively* explain the three experimental observations.

*4.1.2. Incorporation into steps from the surface following serial volume and surface diffusion* [44,45]. In this case the characteristic length of surface diffusion $\lambda$ should be greater than half the biggest interstep distance at which we have observed step field overlap. From the $p_{low} = h/\ell = 6 \times 10^{-3}$ (h is the elementary step height ≈ 100 Å for lysozyme {110} faces) obtained in the etching experiments, $\ell \approx 1.6$ μm. Hence, for surface diffusion field overlap to occur, $\lambda$ must exceed 0.8 μm, which is about 80 unit cell lengths.

In order to obtain for this growth mode a relation that can be readily compared with Eqs. (1) and (2), we make the following assumptions: We assume that the characteristic length for volume-surface exchange of adunits (also referred to "impedance of the adsorption reaction), $\Lambda = a \exp(\Delta E_v/kT)$ , ($a$ is approximately the diameter of a solute molecule, and $\Delta E_v$ the difference between the energy barrier for adsorption on the surface and the activation energy for volume diffusion jumps) is large compared to the mean diffusion distance of admolecules on the surface, $\lambda$. With the above estimate for $\lambda$, this inequality requires that $\Delta E_v \geq 20$ kJ/mol, which is reasonable. Under this condition, Eq. (3.7) in Ref. [44], for incorporation following serial volume and surface diffusion, in the limit of step field overlap, can be simplified to

$$v = \frac{b_{step}\,\sigma}{1 + k\,p} \quad , \tag{3}$$

where $b_{step} = \lambda^2 D\Omega C/\Lambda\Lambda_S h$ is an effective step kinetic coefficient and $k\,p = (\lambda^2/\Lambda_S h)(1 + \delta/\Lambda)p$ is a Peclet number characterizing the importance of the sequential bulk and surface diffusion for step propagation. In this case the requirement for step field overlap $kp \sim 1$ is equivalent to the assumption that the characteristic length for surface-step exchange, $\Lambda_S = a \exp(\Delta E_S/kT)$, with $\Delta E_S$ the difference between the activation energies for step incorporation and surface diffusion jumps, is comparable to or smaller than $\lambda$. Again, this appears reasonable, since it requires that $\Delta E_S \leq 12$ kJ/mol.

Note that the above does not represent evidence for the validity of the surface diffusion mechanism for our system. For this we would have to carry out a critical experiment which can provide different results in the cases of direct incorporation or surface diffusion, for instance in the presence of forced solution flow. These considerations only show that the surface diffusion hypothesis is better *quantitatively* compatible with the available experimental observations.

Note also that Eq. (3) is the same as Eq. (2) if $b_{step} = \beta_{step}\Omega C$, and $k\,p = (\beta_{step}\delta/D)p$. Thus, the following considerations for the interface shape in the presence of step field overlap can also be applied to systems where growth proceeds after the mechanism described in Sect. 4.1.1.

*4.1.3. Interface shape with step field overlap.* With Eq. (3), denoting c for center and e for edge, we can get for a uniform $R = p\,v$ when

$$\frac{p_c\,\sigma_c}{1 + k\,p_c} = \frac{p_e\,\sigma_e}{1 + k\,p_e} \quad . \tag{4}$$

With the supersaturation ratio $q = \sigma_e/\sigma_c$, from here we get

$$p_c = q\,\frac{p_e}{1 - k\,p_e(q - 1)} \quad . \tag{5}$$

Since $q > 1$ and, in the case of step field overlap, $k = O(10^3)$, with $10^{-3} < p_e < 10^{-2}$, $kp_e(q - 1) \rightarrow 1$ and for relatively small supersaturation nonuniformities, $p_c$ may take on considerably larger values than $p_e$. For a numerical treatment of the experimental findings, based on this model combined with actual transport calculations, see our companion paper [42].

The capability of the above model to quantitatively reproduce our experimental findings once again strongly suggests the presence of (surface diffusion) step field overlap in our growth system.

*4.2. Impurity induced growth shape*

For a formal description of this effect, let us assume that impurities influence step motion by adsorption at kink sites on the steps. Experimental support for this assumption can be found in Fig. 10 in Ref. [24]. It shows that at high supersaturations the tangential velocities at the center increase much more with $\sigma$ (and, hence, with R) than at the edge, where we expect higher impurity availability. At high $\sigma$'s, the impurities that impede growth through adsorption on terraces

between steps can be expected to be no longer active [53-55], as can be seen for lysozyme from the same growth rates obtained by different authors with different source materials [20,29].

Next, we assume that the surface concentration of the impurities is proportional to their interfacial solution concentration $C_i$. This corresponds to the linear part of a Langmuir adsorption isotherm at low adsorbate concentrations (see, for instance, Ref. [56]). Since steps are linear objects, the distance between kinks unoccupied by impurity molecules, $\lambda_{kink,i}$ , will increase proportionally to the impurity surface concentration. Hence, $\lambda_{kink,i} \sim C_i$. On the other hand, the step kinetic coefficient is typically inversely proportional to $\lambda_{kink}$ [51,57]. Thus, we relate the effective kinetic coefficients in the presence and absence of impurities, $b_{step,i}$ and $b_{step,0}$, respectively by $b_{step\,i} = b_{step,0}\,(1 + \xi\, C_i)^{-1}$ , where $\xi$ is a phenomenological coefficient characterizing the impurity action. With this $b_{step,i}$ we can rewrite Eq. (3) to

$$v(C_i) = \frac{b_{step,0}}{1 + \xi\, C_i}\,\frac{\sigma}{1 + kp} \quad , \tag{6}$$

From here, for the slope at the facet center we again come to Eq. (5), but the effective supersaturation ratio q now is

$$q_i = \frac{\sigma_e}{\sigma_c}\,\frac{1 + \xi C_{i,c}}{1 + \xi C_{i\,e}} \quad . \tag{7}$$

As noted in Sect 3.2, impurity concentration nonuniformity should be more pronounced than lysozyme nonuniformity, with $C_{i,c}$ being smaller than $C_{i,e}$. Thus, if $\xi$ is sufficiently large so that $\xi C_i = O(1)$, we get $q < 1$ and, from Eq. (5), $p_c < p_e$.

The above formalism can be used for estimating the slope difference between any pair of points belonging to the same step train. If the solute and impurity nonuniformities are comparable in magnitude, (q - 1) may change sign along the facet. This could explain the p increase close to the facet corner followed by a decrease farther inwards, observed in Fig. 7c, Sect. 3.3.

Although the interface shape in both the pure and the impurity influenced case can be described by Eq. (5), there is a certain difference in its physical meaning. If $q > 1$, in the pure case, with $p_e$ sufficiently high but still finite, $p_c$ can tend to infinity. In reality, this would mean that the facet looses stability and a macroscopic depression is formed in the center [5-19,21-23].

With $q < 1$, $p_c$ is always a finite function of $p_e$. In other words, the impurities, if they act in the manner described here, have a stabilizing effect on the growth of polygonal crystals.

## 5. Conclusions

We have investigated the growth morphology and kinetics of tetragonal lysozyme crystals in unstirred solutions with characterized protein composition. We have shown that the presence of less than 1% of high MW protein impurities can lead to a different shape of the growth interface.

In solutions that do not contain protein impurities with MW > 30,000, the growing interface attains convex shapes: the vicinal slope is higher at the facet center than at the edge. This effect increases with increasing crystal size and growth rate. Based on the interface supersaturation distribution calculated in our previous work, we found that the experimentally observed low ratio of the slopes at the edge and center of a facet can be only accounted for by assuming strong overlap of the surface diffusion fields of growth steps.

In solutions containing higher molecular weight protein impurities that are incorporated into the crystal during growth, the shape of the interface is concave: the vicinal slope is higher at the facet edge than at the center. The dependence of this effect on crystal size corroborates its relation to transport-induced impurity nonuniformities at the interface. Since the supersaturations required to obtain concave interface shapes are much higher than the initial "dead" zone, we may conclude that impurities decelerate steps by adsorbing into kinks. Based on this hypothesis, the observed ratios of the vicinal slope at the edge and at the center of a facet can be readily obtained theoretically assuming reasonable values of the governing parameters.

## Acknowledgments

Support for this work by NASA (Grant # NAG8-950), NSF (Grant # DMB-9104630) and the State of Alabama through the Center for Microgravity and Materials Research at the University of Alabama In Huntsville, is gratefully acknowledged. We also thank Mary Alpaugh for the protein purity analyses. Some of the ideas behind Eq. (5) originated in discussions of P.G.V. with Prof. C. Nanev of the Institute of Physical Chemistry, Bulgarian Academy of Sciences.

## References


1. S.P.F. Humphreys-Owen, Proc. Roy. Soc. A, 197 (1949) 218.
2. A. Seeger, Phil. Mag. 44 (1953) 348.
3. W.R. Wilcox, J. Crystal Growth 37 (1977) 229.
4. W.R. Wilcox, J. Crystal Growth 38 (1977) 73.
5. H. Lin, F. Rosenberger, J.I.D. Alexander and A. Nadarajah, J. Crystal Growth, in press.
6. A.A. Chernov, Soviet Phys. - Crystallogr. 16 (1972) 734.
7. A.A. Chernov, J. Crystal Growth 24/25(1974) 11.
8. A.A. Chernov, Modern Crystalography III, Growth of Crystals (Springer, Berlin, 1984) p. 234.
9. T. Kuroda, T. Irisawa and A. Ookawa, J. Crystal Growth 42 (1977) 41.
10. C. Kumar and J. Estrin, J. Crystal Growth 51 (1981) 323.
11. H. Narayanan, G.R. Youngquist and J. Estrin, J. Colloid Interface Sci. 85 (1982) 319.
12. A.M. Ovrutskii and L.M. Chuprina, Soviet Phys.-Cryst. 22 (1977) 393.
13. A.M. Ovrutskii, Soviet Phys.-Cryst. 24 (1979) 327.
14. A.A. Chernov and T. Nishinaga, in: Morphology of Crystals, Ed. I Sunagawa (Terra, Tokyo, 1987) ch. 3, p. 207.
15. C. Nanev, Crystallography Reviews 4 (1994) 3.
16. C. Nanev, J. Crystal Growth 121 (1992) 218.
17. [8], p. 123.
18. C. Nanev and D. Iwanov, J. Crystal Growth 3/4 (1968) 530.
19. C. Nanev, J. Crystal Growth 112 (1991) 235.
20. L.A. Monaco and F. Rosenberger, J. Crystal Growth 129 (1993) 465.
21. R.F. Xiao, J.I.D. Alexander and F. Rosenberger, Physical Review A, 38(5) (1988) 2447.
22. R.F. Xiao, J.I.D. Alexander and F. Rosenberger, J. Crystal Growth 100 (1990) 313.
23. R.F. Xiao, J.I.D. Alexander and F. Rosenberger, Physical Review A, 43(6) (1991) 2977.
24. P.G. Vekilov, L.A. Monaco and F. Rosenberger, J. Crystal Growth, in press.

25. F. Rosenberger, S.B. Howard, J.W. Sowers and T. Nyce, J. Crystal Growth 129 (1993) 1.

26. J.C. Janson and L. Ryden, Protein Purification: Principles, High Resolution Methods and Applications (VCH, New York, 1989) p. 442.

27. J.G. Davis, C.J. Mapes and J.W. Donovan, Biochemistry 10 (1971) 39.

28. A.C. Awade, S. Moreau, D. Molle, G. Brulle, J.-L. Maubois, J. Chromatography A 677 (1994) 279

29. P.G. Vekilov, Progr. Crystal Growth Characterization 26 (1993) 25.

30. P.G. Vekilov and F. Rosenberger, in preparation.

31. S.D. Durbin and G. Feher, J. Mol. Biol. 212 (1990) 763.

32. S.D. Durbin and W.E. Carlson, J. Crystal Growth 122 (1992) 71.

33. S.D. Durbin, W.E. Carlson and M.T. Saros, J. Phys. D: Appl. Phys. 26 (1993) B 128.

34. E. Bauser and H. Strunk, J. Crystal Growth 51 (1981) 362.

35. J.N. Sherwood and T. Shripathi, J. Crystal Growth 88 (1988) 358.

36. J.N. Sherwood and T. Shripathi, Faraday Discuss. 95 (1993) 173.

37. F.C. Frank, J. Crystal Growth 51 (1981) 367.

38. L.J. Gilling and B. Dam, J. Crystal Growth 67 (1984) 400.

39. General Discussion, Faraday Discuss. 95 (1993) 253.

40. L.N. Rashkovich and B.Yu. Shekunov, J. Crystal Growth 100 (1990) 133.

41. P.G. Vekilov and Yu.G. Kuznetsov, J. Crystal Growth 119 (1992) 248.

42. H. Lin, P.G. Vekilov and F. Rosenberger, in preparation.

43. W.K. Burton, N. Cabrera and F.C. Frank, Phil. Trans. Roy. Soc. London A243 (1951) 299.

44. G.H. Gilmer, R. Ghez and N. Cabrera, J. Crystal Growth 8 (1971) 79.

45. J.P. van der Eerden, J. Crystal Growth 56 (1982) 174.

46. A.A. Chernov and A.J. Malkin, J. Crystal Growth 92 (1988) 432

47. P.G. Vekilov, Yu.G. Kuznetsov and A.A. Chernov, J. Crystal Growth 102 (1990) 706.

48. J. Hirth and G. Pound, J. Chem. Phys 26 (1957) 1216.

49. H.Z. Cummins and E.R. Pike, NATO Advanced Study Institutes Series B, vol. 3 (Plenum, New York, 1974) p. 285.

50. A.A. Chernov, V.F. Parvov, M.O. Kliya, D.V. Kostomarov and Yu.G. Kuznetsov, Soviet Phys. Crystallogr. 26 (1981) 640.

51. A.A. Chernov, Soviet Phys. - Uspekhi 4 (1961) 116.

52. M. Muschol and F. Rosenberger, in preparation.

53. N. Cabrera and D.A. Vermileya, in: Growth and Perfection of Crystals, Eds. R.H. Doremus, B.W. Roberts and D. Turnbull (Wiley, New York, 1958) p. 393.

54. V.V. Voronkov and L.N. Rashkovich, Soviet Phys. - Crystallogr. 37 (1992) 289.

55. V.V. Voronkov and L.N. Rashkovich, J. Crystal Growth 144 (1994) 107.

56. P.W. Atkins, Physical Chemistry (Freeman, New York, 1982) p. 1023.

57. Ref. [8], p. 161.

**Figure captions**

Fig. 1. Effect of nonuniform concentration distributions on vicinal slope p illustrated through the motion of a pair of steps. Initial step position indicated by the solid contour. Dashed lines represent pair position near facet center at a later time. The plots represent the solute supersaturation $\sigma$, impurity concentration $C_i$ and resulting step velocity distribution v. (a) In pure solutions, the step spacing at the edge, $\ell_e$, decreases to $\ell_c$ at the facet center. (b) In solutions containing step propagation-impeding impurities, $\ell_e < \ell_c$.

Fig. 2. Protein composition of lysozyme solutions before crystallization, supernatant and dissolved crystals. SDS PAGE analyses with silver staining. Each lane loaded with 8 μg protein.

Fig. 3. Morphology of a (110) lysozyme facet growing from a Seikagaku solution at $\sigma = 2.6$ (T = 14 $^{o}$C). (a) Interferogram; dashed line indicates edge of viewing field (rather than edge of facet). (b) Height profile along the line shown in (a) with arrows indicating local step motion direction. (c) Vicinal slope along the line.

Fig. 4. Development of the convex shape of a (110) face of a crystal growing from a Seikagaku solution. Facet width *a*, supersaturation $\sigma$, average growth rate R, vicinal slope at the edge $p_e$ and the ratio of $p_e$ to slope at center $p_c$ are given for each subfigure. Locations of $p_e$ and $p_c$ measurements (always made in the direction of local fringe motion) indicated by (x). Dashed lines indicate edges of viewing field.

Fig. 5. Morphology of a (110) face growing from a Sigma solution at $\sigma = 2.35$ (T = 16 $^{o}$C). (a) Interferogram; dashed lines indicate edge of viewing field. (b) Concave height profile along the line shown in (a) with arrows indicating step motion directions. (c) Vicinal slope along line.

Fig. 6. Development of the morphology of a (110) face growing from a Sigma solution at $\sigma$ = 2.8 (T = 12 $^{o}$C). Facet width *a*, supersaturation $\sigma$, average growth rate R, vicinal slope at the edge, $p_e$, and the ratio of $p_e$ to the slope at center, $p_c$, are given for each subfigure. Locations of $p_e$ and $p_c$ measurements indicated by (x). Dashed lines indicate edge of viewing field.

Fig. 7. Development of the morphology of a (110) face growing from a Sigma solution. Facet width *a*, supersaturation $\sigma$, average growth rate R, vicinal slope at the edge $p_e$ and the ratio of vicinal slope at edge to slope at center $p_c$ are given for each subfigure. Locations of $p_e$ and $p_c$ measurements indicated by (x). Dashed lines indicate edge of viewing field.

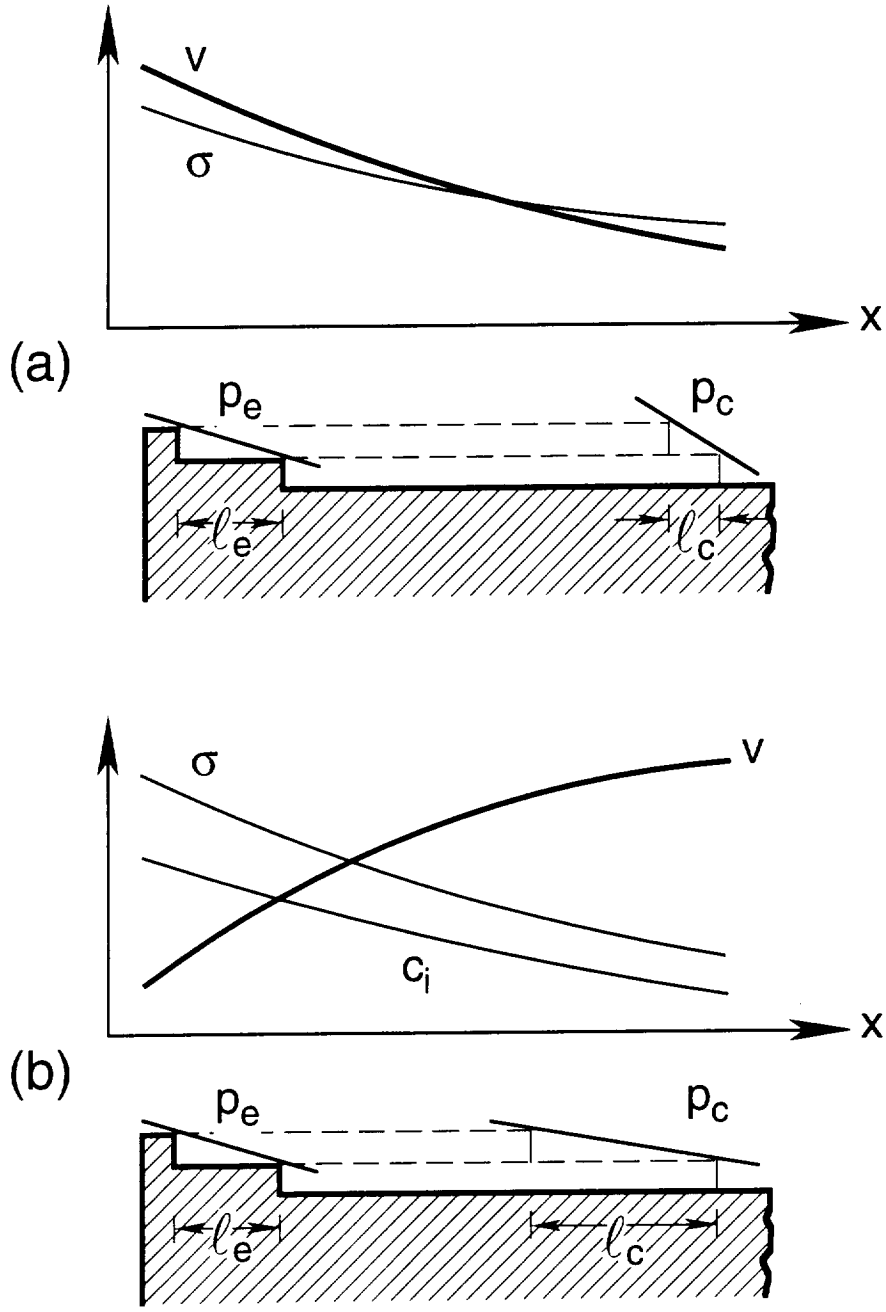


FIG. 1

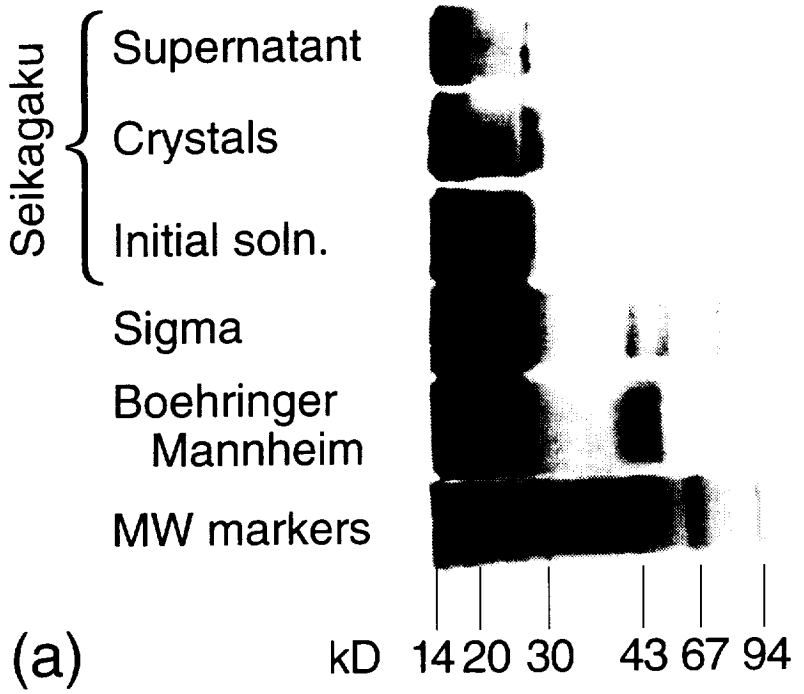
Seikagaku
Supernatant
Crystals
Initial soln.
Sigma
Boehringer Mannheim
MW markers
kD 14 20 30 43 67 94

(a)

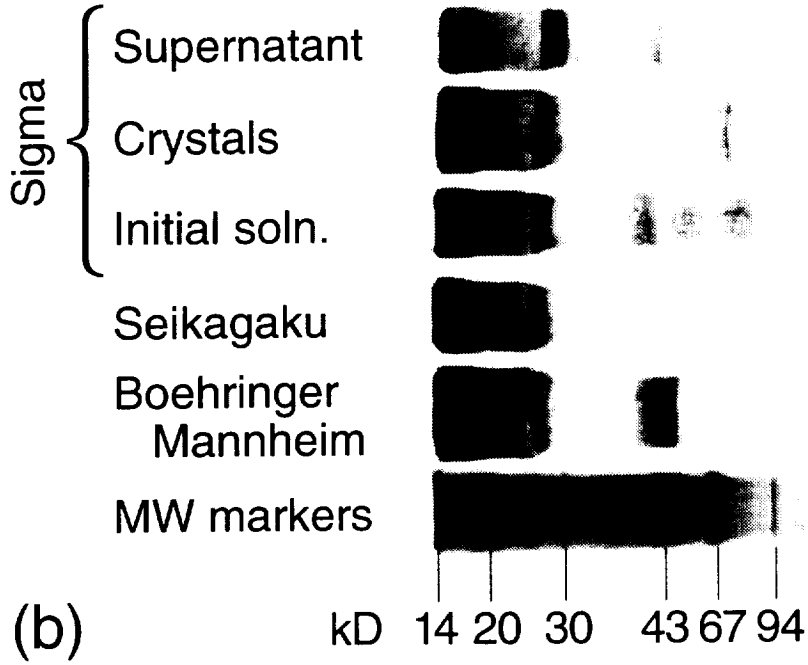
Sigma
Supernatant
Crystals
Initial soln.
Seikagaku
Boehringer Mannheim
MW markers
kD 14 20 30 43 67 94

(b)

FIG. 2

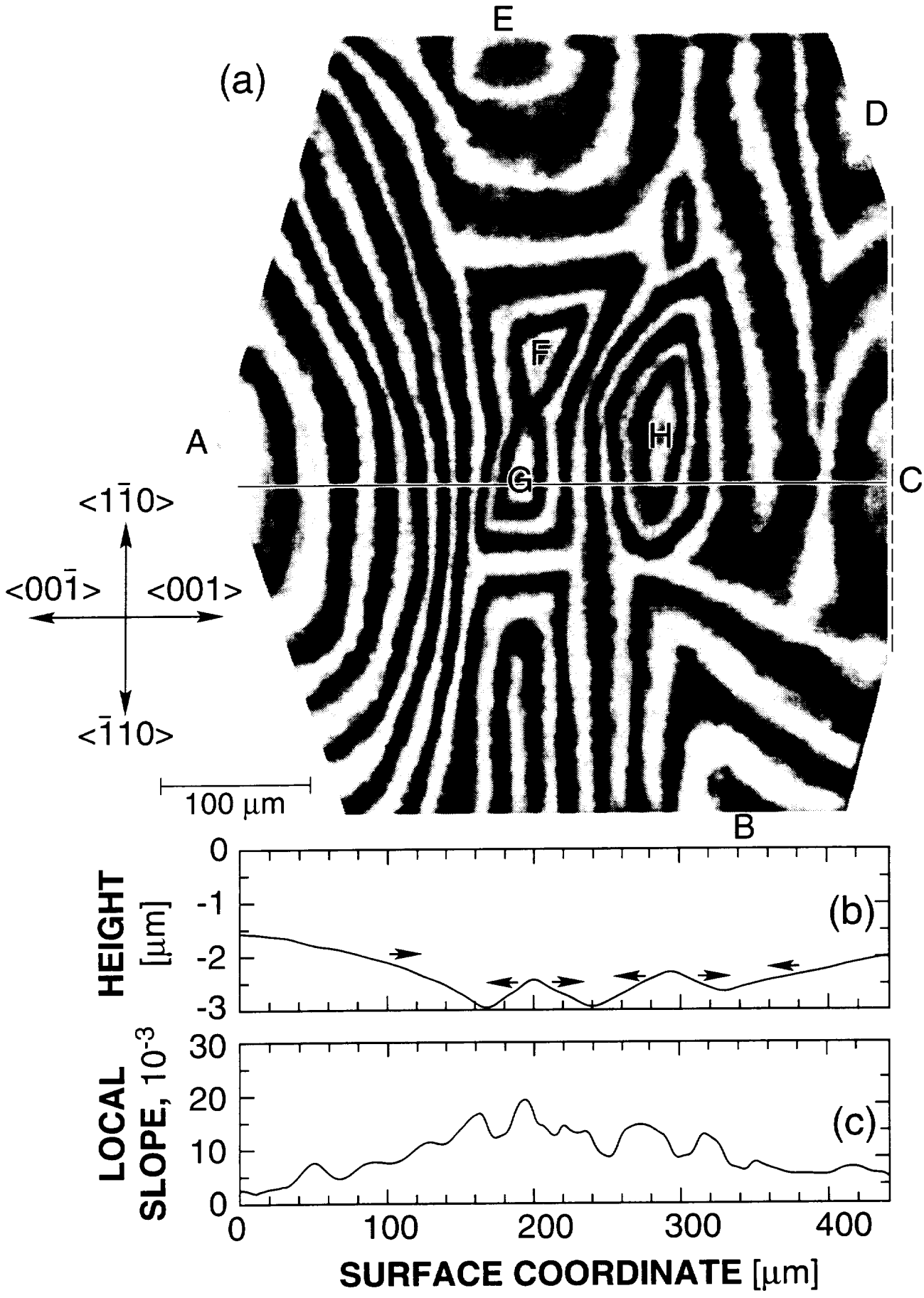
E
(a)
D
A
C
B
F
G
H
<1$\bar{1}$0>
<00$\bar{1}$>
<001>
<$\bar{1}$10>
100 µm
HEIGHT [µm]
0
-1
-2
-3
(b)
LOCAL SLOPE, $10^{-3}$
30
20
10
0
(c)
0
100
200
300
400
SURFACE COORDINATE [µm]

FIG. 3

a = 258 μm, σ = 2.84
R = 8.1 Å/s, $p_e = 2.9\times10^{-3}$
$p_e/p_c = 1.2$

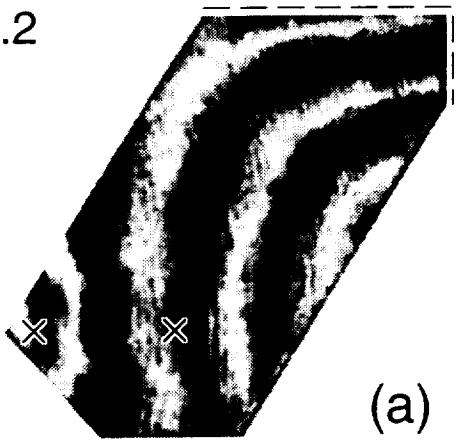

(a)

a = 337 μm, σ = 1.80
R = 1.2 Å/s, $p_e = 1.7\times10^{-3}$
$p_e/p_c = 1.2$

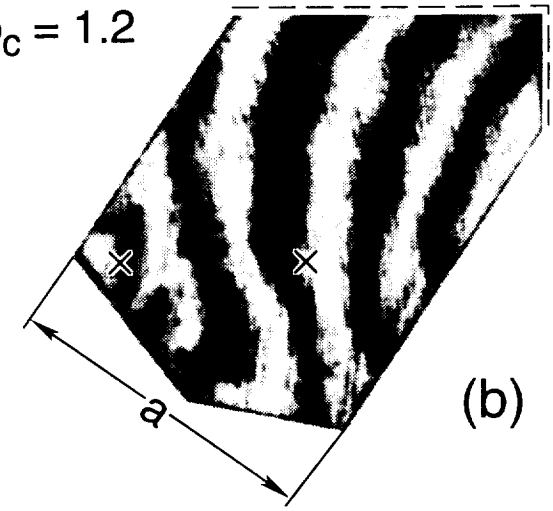


(b)

a = 357 μm, σ = 2.84
R = 8.2 Å/s, $p_e = 2.9\times10^{-3}$
$p_e/p_c = 0.61$

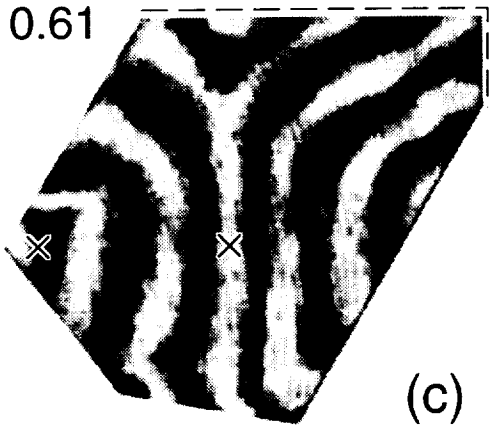

(c)

a = 364 μm, σ = 2.84
R = 5.5 Å/s, $p_e = 2.2\times10^{-3}$
$p_e/p_c = 1.1$

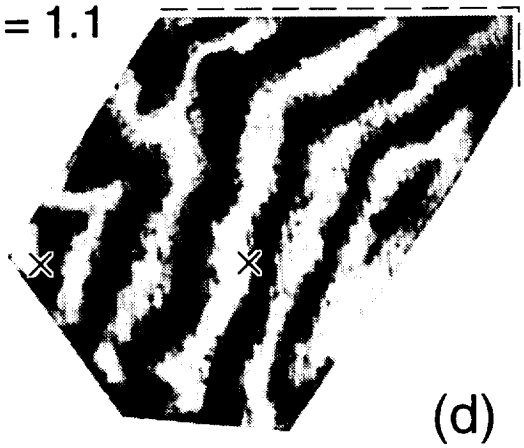

(d)

a = 411 μm, σ = 1.80
R = 1.6 Å/s, $p_e = 3.2\times10^{-3}$
$p_e/p_c = 1.9$

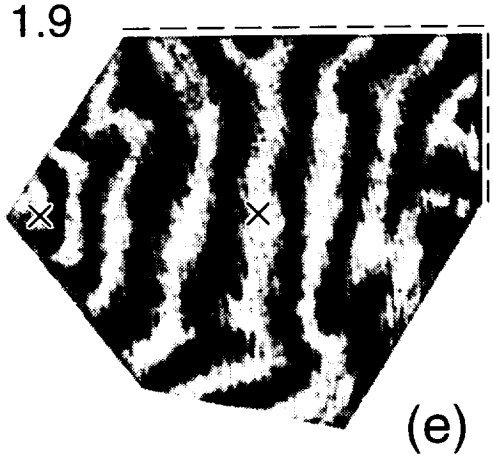

(e)

a = 437 μm, σ = 2.84
R = 7.5 Å/s, $p_e = 2.7\times10^{-3}$
$p_e/p_c = 0.41$

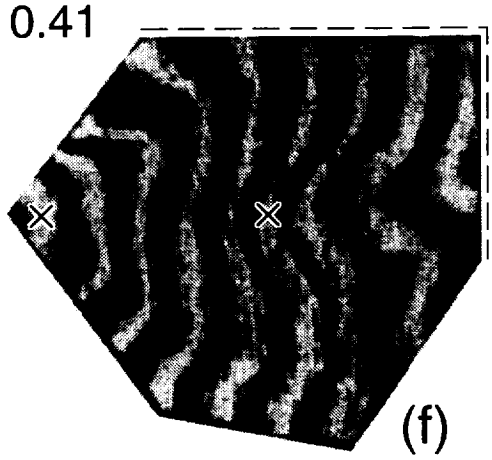

(f)

100 μm

FIG. 4

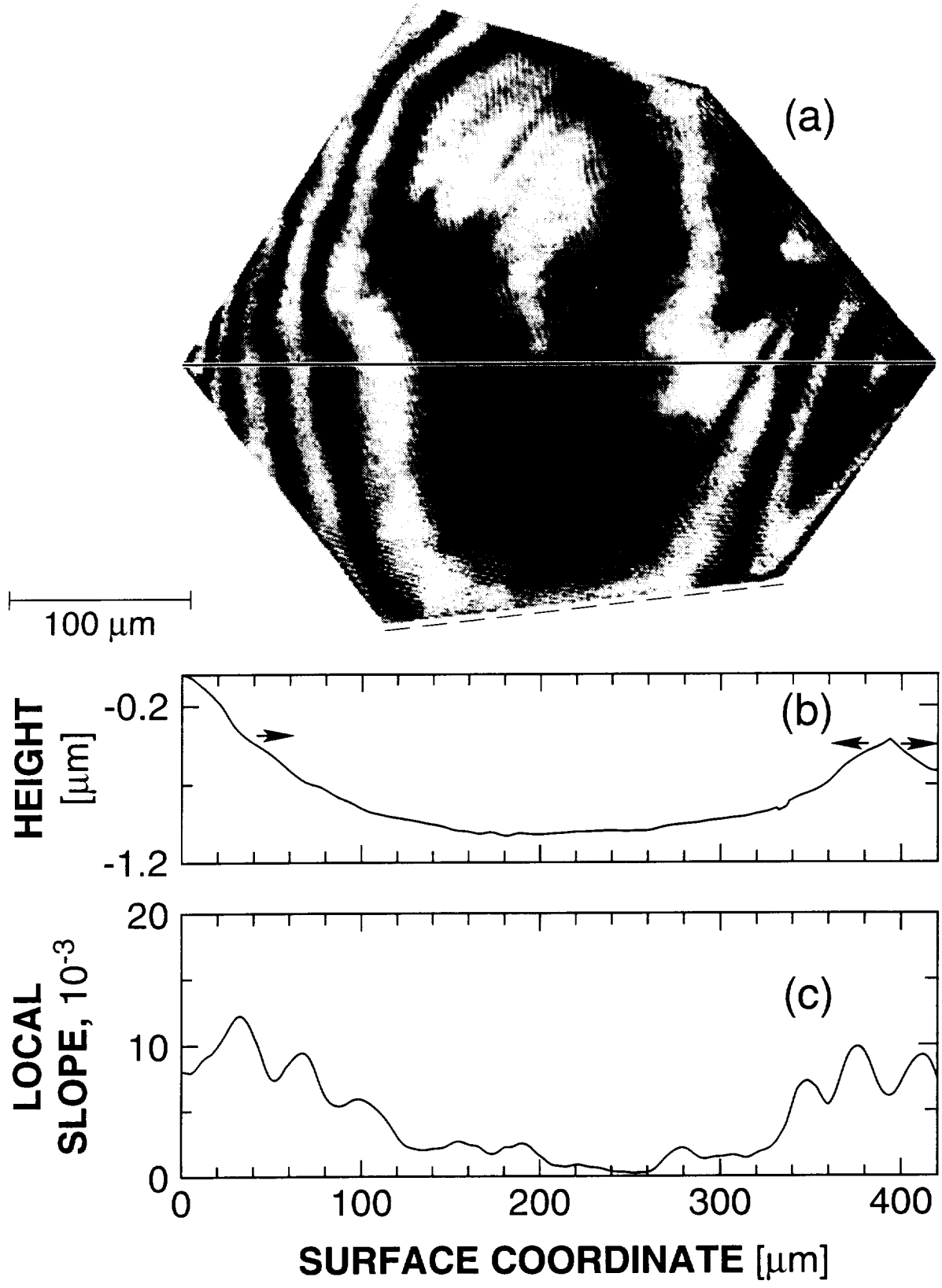
(a)
100 μm
HEIGHT [μm]
-0.2
-1.2
(b)
LOCAL SLOPE, $10^{-3}$
20
10
0
(c)
0
100
200
300
400
SURFACE COORDINATE [μm]

FIG. 5

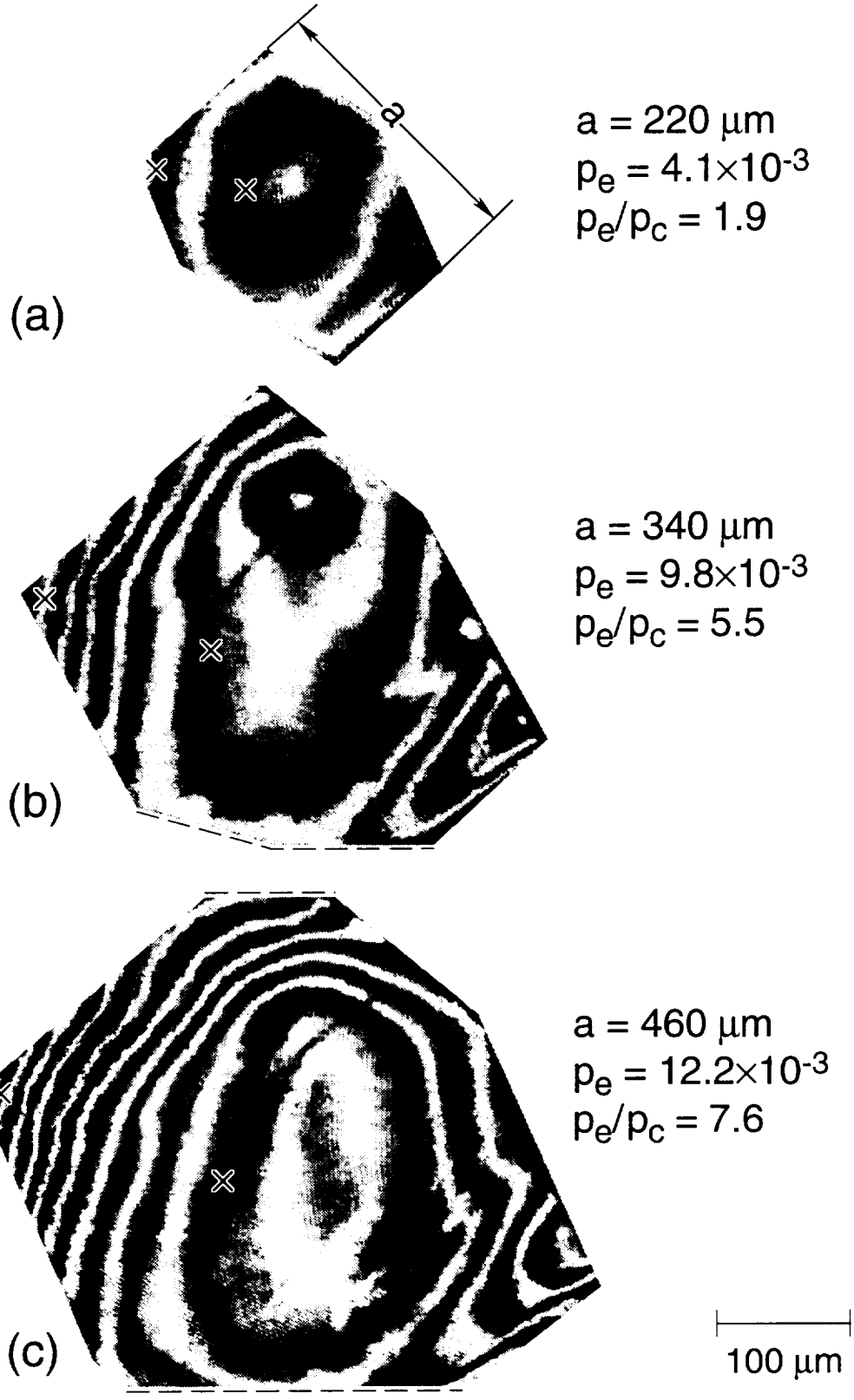
a
a = 220 μm
$p_e = 4.1\times10^{-3}$
$p_e/p_c = 1.9$
(a)
a = 340 μm
$p_e = 9.8\times10^{-3}$
$p_e/p_c = 5.5$
(b)
a = 460 μm
$p_e = 12.2\times10^{-3}$
$p_e/p_c = 7.6$
(c)
100 μm

FIG. 6

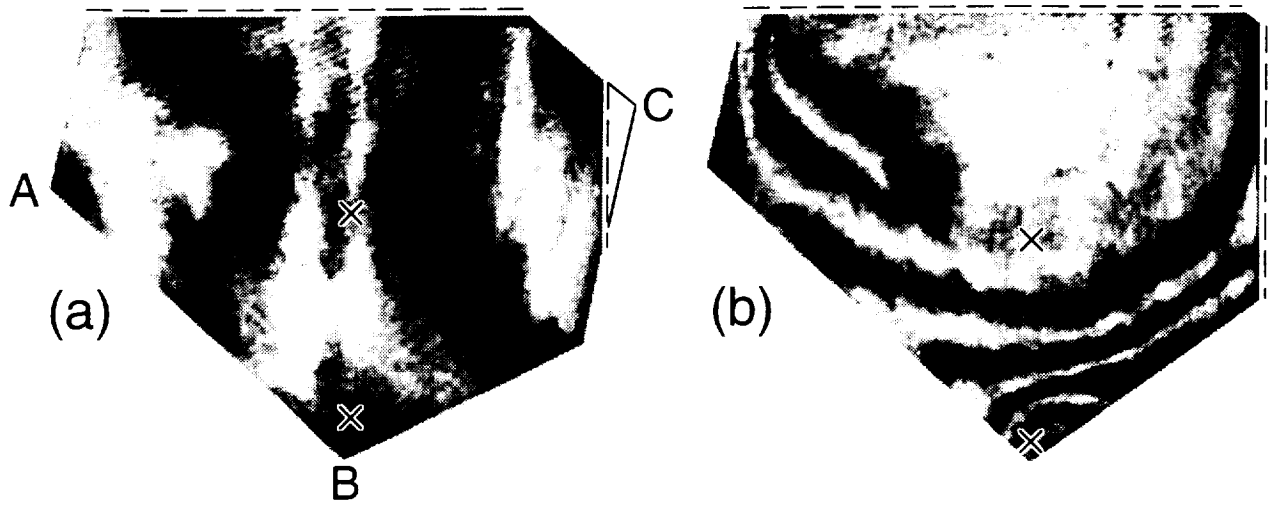


a = 427 μm, σ = 1.13
R = 2.0 Å/s, $p_e = 1.8\times10^{-3}$
$p_e/p_c = 1.2$

a = 455 μm, σ = 1.81
R = 8.7 Å/s, $p_e = 8.1\times10^{-3}$
$p_e/p_c = 4.0$

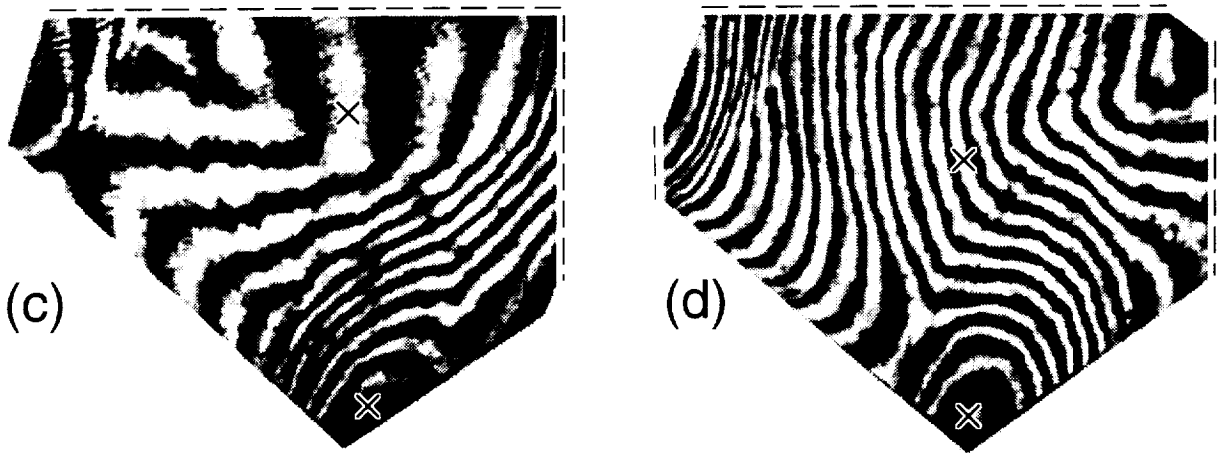


a = 462 μm, σ = 2.38
R = 11.4 Å/s, $p_e = 6.1\times10^{-3}$
$p_e/p_c = 2.7$

a = 463 μm, σ = 3.24
R = 10.3 Å/s, $p_e = 4.6\times10^{-3}$
$p_e/p_c = 0.57$

100 μm

FIG. 7